ENGINYERIA ELECTRÒNICA ELÈCTRICA I AUTOMÀTICA

UNIVERSITAT ROVIRA I VIRGILI

Graduate Students Meeting on Electronics Engineering

Tarragona, June 29th and 30th, 2020

BOOK OF ABSTRACTS

IEEE

ENGINYERIA ELECTRÒNICA ELÈCTRICA I AUTOMÀTICA

UNIVERSITAT ROVIRA I VIRGILI

Graduate Students Meeting on Electronics Engineering

Tarragona, June 29th and 30th, 2020

PROGRAM

Monday, June 29th:

9.00 - Opening

9.10 – Maria Alba (Monash University)

10.00 – José Guadalupe Sánchez (Institut Català d'Investigació Química)

15.00 – Paul Berger (Ohio State University)

16.00 – Ph. D. Students Oral Presentations

- Carla Merino - Exposure to Thirdhand Smoke induces developmental and metabolic changes in zebrafish embryos

- Aristeidis Nikolaou - Statistical Circuit Analysis by NOVA (Noise Based Variability Approach)

- Alexandra Iakab - Gold Nanoparticle-Assisted Black Silicon Substrates for Mass Spectrometry Imaging Applications

- Alfonsina Abat - Impedance Spectroscopy Analysis of Indoor Organic Solar Cells: A Study Case

18.30 – Francesc Fons (Huawei Technologies – Munich Research Center)

Tuesday, June 30th:

9.00 – Abel Santos (University of Adelaide)

15.00 - Paul Berger (Ohio State University) - wrap-up and Q&A

16.00 – Roger Mallol (La Salle - Universitat Ramon Llul)

17.00 - Juan Francisco Méndez (Universidad Pública Autónoma del Estado de Puebla)

18.00 - Closing

ENGINYERIA ELECTRÒNICA ELÈCTRICA I AUTOMÀTICA

UNIVERSITAT ROVIRA I VIRGILI

Graduate Students Meeting on Electronics Engineering

Tarragona, June 29th and 30th, 2020

STUDENTS PROCEEDINGS

Statistical Circuit Analysis by NOVA (Noise Based Variability Approach)

Aristeidis Nikolaou, Jakob Leise, Jakob Pruefer, Ghader Darbandy, Benjamin Iñiguez, Alexander Kloes

***Abstract*—The current study presents an accurate and time saving circuit-based DC statistical analysis methodology, tested in basic organic thin-film transistor circuit topologies. The proposed Noise Based Variability Approach can be used versus traditional Monte Carlo analysis to determine accurately the variation on DC characteristics caused by statistical variations on the device basic parameters.**

I. Introduction

Process variability introduces variations on the transistor main electrical parameters and is considered to be one of the main factors limiting the down-scaling of conventional silicon CMOS technologies [1]. Similarly, parameter variations as a source of variability, such as threshold voltage, mobility and dimensions variations, on organic thin-film transistors (OTFTs) is currently under investigation [2]. Monte Carlo (MC) simulation is commonly used to determine the performance of OTFT based circuits versus parameter variability [3]. In the current paper an alternative to MC method namely "Noise Based Variability Approach" (NOVA) will be presented.

II. Devices and Measurements

The experimental devices population comprises 16 nominally identical p-type OTFTs, fabricated on a flexible polyethylene naphthalate (PEN) substrate of $125\,\mu m$ thickness, with 2,9-didecyl-dinaphtho[2,3-b:2′,3′-f]thieno[3,2-b]thiophene (C_{10}-DNTT) accounting for the organic semiconductor material. All transistors have identical channel widths and channel lengths of $10\,\mu m$ and $1\,\mu m$, respectively. The exact fabrication procedure is described thoroughly in [4]. For every sample, the measurement protocol consists of transfer characteristics at $V_{DS} = -2.0\,V$. Gate voltage spans from $V_{GS} = 0\,V$ down-to $V_{GS} = -2.0\,V$.

III. Compact Modeling of OTFTs

The OTFT charge-based model described in [5] was applied to the measured data. The proposed model provides a single

This project is funded by the German Federal Ministry of Education and Research ("SOMOFLEX", No. 13FH015IX6) and the German Research Foundation (DFG) under the grant KL 1042/9-2 (SPP FFlexCom). We would like to thank U. Zschieschang and H. Klauk (Max Planck Institute for Solid State Research, Stuttgart 70569, Germany) for the provision of measurement data and AdMOS GmbH for support.

A. Nikolaou, J. Leise, J. Pruefer, G. Darbandy and A. Kloes are with NanoP, TH Mittelhessen University of Applied Sciences, 35390 Giessen, Germany (e-mail: aristeidis.nikolaou@ei.thm.de). A. Nikolaou, J. Leise, J. Pruefer and B. Iniguez are with DEEEA, Universitat Rovira i Virgili, Tarragona, Spain.

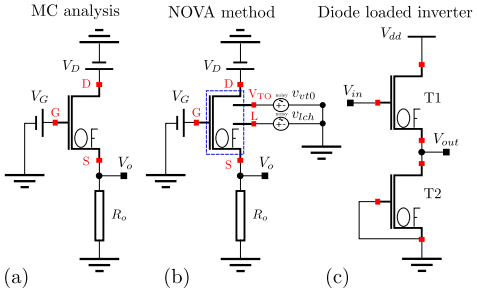

Figure 1. (a) Source follower schematic comprises an instance of a Verilog-A 3-terminal p-type OTFT, two DC voltage sources and an output resistor $R_o = 1\,\Omega$. (b) Identical circuit topology as in (a) with the difference that the transistor instance is replaced by a 5-terminal OTFT structure. In the two additional terminals, alternating "noisy" voltage sources are connected in order to modify threshold voltage ($vt0$) and channel length (lch) Verilog-A parameters, according to the proposed NOVA method. (c) Diode loaded inverter topology consisting of two p-type OTFTs with $W/L = 10\,\mu m/1\,\mu m$ and $V_{dd} = 2.0\,V$.All simulations are performed in Cadence Virtuoso ADE.

current equation valid for all operation regions that can be obtained from

$$I_{DS} = \mu_{eff} W_{ch} \left(\frac{kT}{q} \frac{Q'_{mS} - Q'_{mD}}{L_{ch}} + \frac{Q'^2_{mS} - Q'^2_{mD}}{2 L_{ch} C'_{ox}} \right) \times \left(1 + \lambda \left(V_{DS} - V_{Dsat}\right)\right), \quad (1)$$

where W_{ch} is the channel width, L_{ch} is the channel length, C'_{ox} is the gate capacitance per gate area, λ is the channel length modulation factor and μ_{eff} is the effective mobility. Q'_{mS} and Q'_{mD} describe the density of quasi mobile charges per gate area at the source and drain end of the channel respectively. The model is available in Verilog-A language. Table I includes the actual values and variations of $vt0$ and

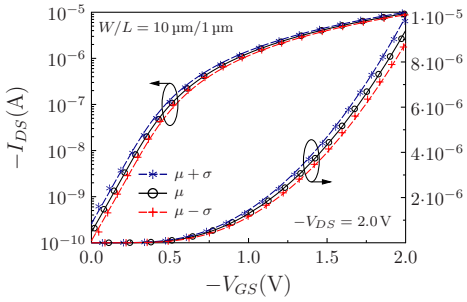

Figure 2. Mean value μ and mean value $\mu \pm \sigma$ drain current I_{DS} versus gate voltage V_{GS}, extracted from a population of 16 different saturated ($V_{DS} = -2.0\,V$) C_{10}-DNTT TFTs of $W/L = 10\,\mu m/1\,\mu m$. Markers: measured data, solid/dashed lines: model.

lch parameters in detail. Fig. 2 shows the mean value μ and mean value $\mu \pm \sigma$ transfer characteristics, out of the 16 different

saturated p-type DNTT TFTs of $W/L = 10\,\mu\text{m}/1\,\mu\text{m}$. In all cases markers denote the measurements whereas solid and dashed lines correspond to the models.

Table I
PARAMETER VARIATIONS OF THE EXTRACTED MODELS

	μ model	$\mu - \sigma$ model	$\mu + \sigma$ model	variation $\times\%$
$vt0$	$-333\,\text{mV}$	$-363\,\text{mV}$	$-304\,\text{mV}$	$\simeq \pm 8.7\%$
lch	$1\,\mu\text{m}$	$1.023\,\mu\text{m}$	$0.975\,\mu\text{m}$	$\simeq \pm 2.5\%$

IV. Noise Based Variability Approach (NOVA)

In this section an alternative to the Monte Carlo method for fast statistical evaluation of OTFT based circuits will be presented. The proposed approach is based on circuit noise simulation principles and can be abbreviated as NOVA (Noise Based Variability Approach). It has to be mentioned that the proposed method can be expanded into any conventional circuit topology.

In simulator based noise analyses, all the spectra of noise contributing circuit components are added to the output port. The result corresponds to the variance of the output port value. Noisy voltage sources can be commonly implemented in Cadence simulator by using an AC voltage source and adding the desirable mean-square value of noise. Alternatively a port instance can be used. In both cases a thermal noise Thevenin equivalent circuit is implemented. The central limit theorem indicates that thermal noise is Gaussian distributed with zero mean [6]. Furthermore, for Gaussian distributed noise, the standard deviation σ is equal to the root-mean-square value of noise [7].

In Fig. 1(b) the circuit used for the proposed method is depicted. NOVA topology is identical with the one used for the MC analysis, with the difference that the transistor instance is replaced by a 5-terminal OTFT structure. In the two additional terminals, alternating "noisy" voltage sources are connected in order to modify threshold voltage ($vt0$) and channel length (lch) Verilog-A parameters. Voltage sources are configured in the following way: The DC voltage value and the mean-square value of noise is equal to the mean value and the variance of $vt0$ and lch parameters, respectively. The OTFT Verilog-A code is updated accordingly. After the circuit is configured, a parametric noise analysis, with respect to the different V_{GS} bias points, is performed. The result at the output is the variance of the signal. This variance is the square of the standard deviation. The standard deviation of the output signal equals to the root-mean-square of the noise distribution.

V. Results and Discussion

Fig. 3 shows the standard deviation of the output current $\sigma(-I_{DS})$ versus the gate voltage V_{GS}. Blue circles describe the standard deviation extracted from the measured data, black line indicates the results after a 5000 iteration MC simulation and red crosses account for the standard deviation of the current extracted from proposed method (NOVA). Both methods describe the circuit bias dependent variability coherently, following identical trend versus the gate biasing conditions. The processing times of NOVA versus MC methods for the tested circuits are listed in Table II. NOVA presents a time improvement close to $99\,\%$ when compared to the typical MC simulation in all cases.

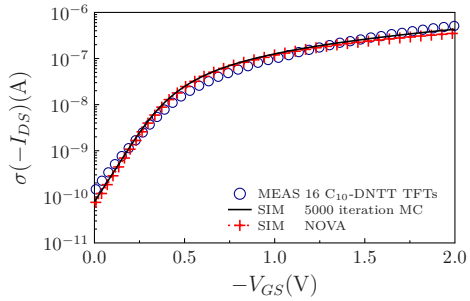

Figure 3. Standard deviation of the output current $\sigma(-I_{DS})$ vs. gate voltage V_{GS}. Blue circles: measurements, line: 5000 point MC analysis, red crosses: proposed method (NOVA).

Table II
SIMULATION PROCESSING TIMES

	5000 MC iterations	NOVA method
Source Follower	$\simeq 201\,\text{min}$	$\simeq 2\,\text{min}$
Inverter mismatch analysis	$\simeq 214\,\text{min}$	$\simeq 2\,\text{min}$
Inverter process variations	$\simeq 202\,\text{min}$	$\simeq 2\,\text{min}$

VI. Conclusions

In conclusion, the current work introduces an alternative to Monte Carlo statistical analysis methodology, tested in OTFT based circuits. The proposed Noise Based Variability Approach (NOVA) can be used for fast process and mismatch statistical circuit analyses. NOVA can be easily implemented through minor changes on Verilog-A transistor instances and fast rearranging of circuit topologies. NOVA can only be used for Gaussian shaped statistical distributions whereas MC can provide other distribution functions as well. The small deviation versus the vast processing time improvement that NOVA presents when compared to the traditional MC simulation, is a trade off that can be beneficial for circuit designers.

References

[1] K. J. Kuhn, "Reducing variation in advanced logic technologies: Approaches to process and design for manufacturability of nanoscale cmos," in *2007 IEEE International Electron Devices Meeting*, Dec 2007, pp. 471–474.

[2] U. Zschieschang, F. Letzkus, J. N. Burghartz, and H. Klauk, "Parameter uniformity of submicron-channel-length organic thin-film transistors fabricated by stencil lithography," *IEEE Transactions on Nanotechnology*, vol. 16, no. 5, pp. 837–841, Sep. 2017.

[3] S. Jacob, S. Abdinia, M. Benwadih, J. Bablet, I. Chartier, R. Gwoziecki, E. Cantatore, A. van Roermund, L. Maddiona, F. Tramontana, G. Maiellaro, L. Mariucci, M. Rapisarda, G. Palmisano, and R. Coppard, "High performance printed n and p-type OTFTs enabling digital and analog complementary circuits on flexible plastic substrate," *Solid-State Electronics*, vol. 84, pp. 167 – 178, 2013.

[4] U. Zschieschang, R. Hofmockel, R. Rödel, U. Kraft, M. J. Kang, K. Takimiya, T. Zaki, F. Letzkus, J. Butschke, H. Richter, J. N. Burghartz, and H. Klauk, "Megahertz operation of flexible low-voltage organic thin-film transistors," *Organic Electronics*, vol. 14, no. 6, pp. 1516 – 1520, 2013.

[5] F. Hain, M. Graef, B. Iñíguez, and A. Kloes, "Charge based, continuous compact model for the channel current in organic thin-film transistors for all regions of operation," *Solid-State Electronics*, vol. 133, pp. 17 – 24, 2017.

[6] S. Haykin, *Communication Systems*, 5th ed. Wiley Publishing, 2009.

[7] K. Feher and H.-P. L. Engineers, *Telecommunications Measurements, Analysis, and Instrumentation*. Noble Publishing Corporation, 1997.

On-Current Influence on the Performance of TFET–Based Circuits using a Compact Model

Atieh Farokhnejad[1,2,✠], Fabian Horst[1,2], Benjamín Iñíguez[2], François Lime[2] and Alexander Kloes[1]
[1]NanoP, TH Mittelhessen University of Applied Sciences, Giessen, Germany,
[2]DEEEA, Universitat Rovira i Virgili, Tarragona, Spain,
[✠]atieh.farokhnejad@ei.thm.de

***Abstract*—Concerning the innovations in architecture of tunnel–field effect transistor (TFET), the potential to achieve higher on–current increases. In respect thereof, the focus of this paper is on an optimized TFET with higher current flowing through its channel and simulating its static and dynamic behavior using a compact model. The scalability of the model allows to estimate the impact of an on–current improvement on the intrinsic speed and switching energy of TFET inverters through scaling their channel length and supply voltage.**

I. Introduction

TFETs are attracting widespread interest due to their feasibility to overcome the 60 mV/dec subthreshold slope of conventional MOSFETs. However, one of the major drawback of TFETs is their low on current [1]. To achieve higher on–current, much work on alternative TFET architecture and different semiconductor materials has been carried out [2]. Among them line tunneling TFET (lt–TFET) seems to be a promising approach to improve the I_{on}/I_{off} ratio. This concept refers to enlargement of the tunneling region. That is to say, in this structure tunneling does not happen only in a small region in source/channel interface, which is known as point tunneling (pt) and is shown in fig. 1(a), but also along the channel in the direction of gate's electric field (see fig. 1(b)). Considering the conceivable role of TFETs in further scaling of integrated circuits (ICs), compact models for characterizing TFET as single element and also to simulate the TFET–based circuits are of growing interest. With all these in mind, in this paper a compact DC model introduced in [3] combined with intrinsic capacitances model in [4], is firstly tailored to an optimized single gate lt–TFET and then it is used to simulate some basic digital circuits.

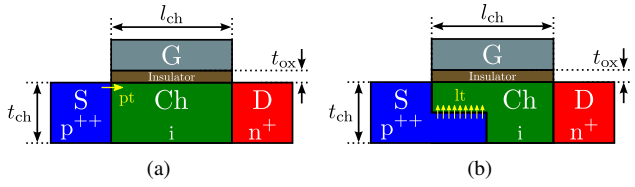

Figure 1. 2D sketch of N–type pt–TFET and lt–TFET. The structural parameters are defined as: l_{ch}=22 nm, t_{ch}=10 nm and t_{ox}=2 nm. For the source, drain and channel silicon and for the gate oxide HfO_2 is used. Source is highly doped ($N_s = 10^{20}cm^{-3}$) and drain has a reduced doping concentration ($N_d = 10^{19}cm^{-3}$), the channel is intrinsic. (a) Point tunneling happens at the source/channel interface under the gate oxide. (b) Line tunneling takes place along the channel elongated with the gate's electric field.

II. Simulation Setup

In the first step, the accuracy of our compact model was investigated by comparing the resulting electrical properties of a single device with those obtained by TCAD Sentaurus. The model is then implemented using Cadence electronic design automation software to simulate a TFET inverter and an 11–stage ring–oscillator. All simulations are performed for both pt–TFET and lt–TFET. The effect of line tunneling is implemented in the compact model by coefficient β. This means, it is considered that the line tunneling simply increases the on–current by factor β. In the case of point tunneling β = 1 and when line tunneling is taken into account, β = 1000. In fig. 2 the transfer curves of N– and P–type TFET for both cases are depicted and fig. 3 presents the inverter and ring–oscillator that are simulated based on these TFETs.

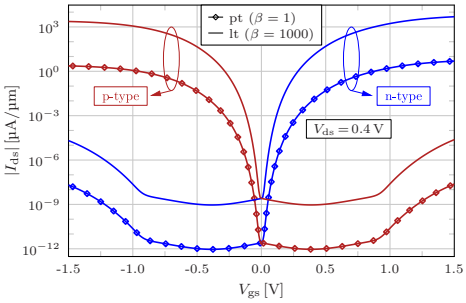

Figure 2. Transfer characteristic of the single gate N– and P–TFET considering line and point tunneling.

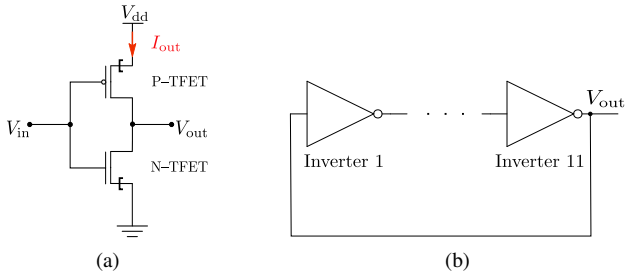

Figure 3. Schematic of digital circuits designed based on TFET: (a) inverter and (b) 11–stage ring–oscillator.

III. Results and Conclusion

In fig. 4 the voltage transfer curve (VTC) and the output current of the inverter are presented (see fig. 3(a)). In initial state V_{in} = 0 V, P–TFET is on and V_{dd} = 0.4 V is connected to V_{out} with a low resistance. Increasing V_{in} from that point also makes the N–TFET to start to conduct and in this moment that both transistors are conducting, a path between V_{dd} and the ground is created. Further increment in V_{in} leads to a decrement of the output voltage V_{out} to 0 V. During the switching event the current flow reaches its maximum. For both pt– and lt–TFET,

the VTC slope is the same. But in the line tunneling case the switching current is proportionally to β higher than the point tunneling case. Consequently, the period (T) of the lt–TFET ring–oscillator is shorter in comparison to the pt–TFET one (see fig. 5).

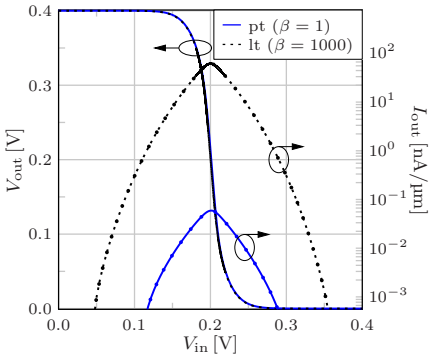

Figure 4. VTC and current curve of TFET inverter for V_{dd} = 0.4 V. Solid lines refer to the point tunneling case and dotted lines address the lt–TFET.

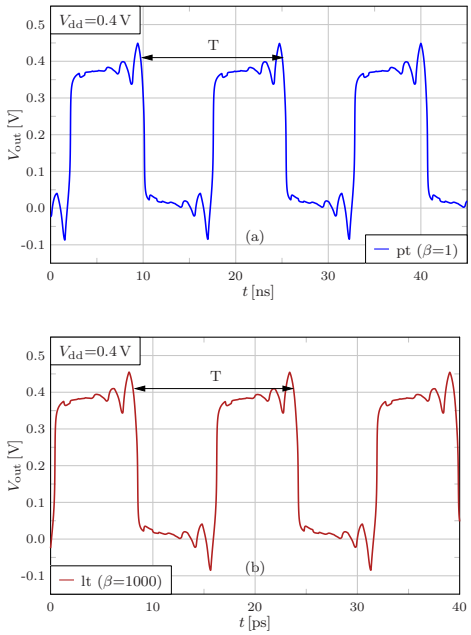

Figure 5. Output waveform of the 11–stage ring–oscillator. T shows the period of one oscillation. In (a) pt–TFET is considered and in (b) lt–TFET ring–oscillator is evaluated.

Figure 6 depicts the dependency of intrinsic inverter delay and the average power consumption of each inverter in the ring–oscillator on supplied voltage (V_{dd}). As expected the lt–TFET inverter, due to high I_{out}, has a shorter intrinsic delay and bigger average power consumption. It can be seen that increasing V_{dd} results in higher power consumption but the inverter delay is not much affected. It seems an increase in TFET on–current due to higher V_{dd} is partially compensated by a larger amount of charge stored in the intrinsic capacitances. In fig. 7 the intrinsic inverter delay for various channel lengths is illustrated. Symbols show the delay calculated as τ= T/2n where n is the number of stages. Furthermore, the corresponding curve for a typical CMOS inverter in 32–nm node with V_{dd} = 0.8 V is plotted [5]. Concerning the fact that in TFETs, the current is independent from channel length, the intrinsic inverter delay is proportional to l_{ch}. In MOSFETs both current and capacitances are affected by channel length and thus, the MOSFET inverter delay is proportional to l_{ch}^2. It can be seen that by taking advantage of line tunneling, the dynamic performance of the TFET is improved in terms of switching pace and becomes competitive to CMOS technology yet with significantly lower supply voltage.

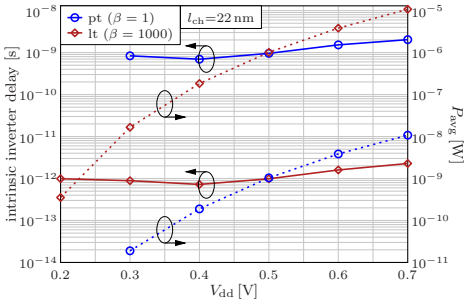

Figure 6. Intrinsic inverter delay and average power consumption in ring–oscillator as a function of V_{dd}.

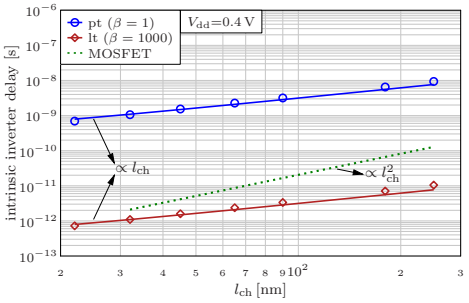

Figure 7. Inverter delay extracted from ring–oscillator circuit as a function of channel length. Symbols refer to the intrinsic inverter delay calculated from the oscillation frequency of the ring–oscillator. Solid lines present the theoretical relation of the intrinsic delay and channel length. Dotted line refers to the similar relation extracted for a CMOS inverter based on standard MOSFETs at V_{dd}=0.8 V.

Acknowledgment

This project was supported by the German Federal Ministry of Education and Research under contract No. FKZ 13FH010IX5 and the Spanish Ministry of Economy and Competitiveness through project GREENSENSE (TEC2015-67883-R). We would like to thank Keysight Technologies for the license donation and support of the software IC-CAP and AdMOS GmbH for their support.

References

[1] E. Gnani, M. Visciarelli, A. Gnudi, S. Reggiani, and G. Baccarani, "TFET inverter static and transient performances in presence of traps and localized strain," *Solid-State Electronics*, 2019 (In Press).

[2] J.-T. Lin, T.-C. Wang, W.-H. Lee, C.-T. Yeh, S. Glass, and Q.-T. Zhao, "Characteristics of recessed-gate TFETs with line tunneling," *IEEE Transactions on Electron Devices*, vol. 65, no. 2, pp. 769–775, feb 2018.

[3] F. Horst, A. Farokhnejad, Q. Zhao, B. Iñíguez , and A. Kloes, "2-D physics-based compact DC modeling of double-gate tunnel-FETs," *IEEE Transactions on Electron Devices*, vol. 66, no. 1, pp. 132–138, Jan 2019.

[4] A. Farokhnejad, M. Schwarz, F. Horst, B. Iñíguez, F. Lime, and A. Kloes, "Analytical modeling of capacitances in tunnel–FETs including the effect of Schottky barrier contacts," *Solid-State Electronics*, 2019 (In Press).

[5] S. I. Association. (2015) International technology roadmap for semiconductors. [Online]. Available: https://www.semiconductors.org/wp-content/uploads/2018/06/0_2015-ITRS-2.0-Executive-Report-1.pdf

Extension of a Charge-Based Compact Model for Intrinsic Charges in Staggered Organic Thin-Film Transistors for Multi-Finger Structures

Jakob Leise, Jakob Pruefer, Ghader Darbandy, Benjamin Iñiguez, Alexander Kloes

***Abstract*—A charge-based approach to calculate the intrinsic charges in staggered organic thin-film transistors is presented. Based on an already existing DC compact model, the charge model has been developed. This charge model has been extended by a model for the fringing regions which appear in fabricated transistors. The final model describes the capacitances based on the geometrical dimensions of the device introducing a fitting parameter which accounts for the current spreading in fringing regions. The model is implemented in Verilog-A and verified using Sentaurus TCAD simulation results.**

I. Introduction

Organic semiconductors (OSCs) have gained lots of interested due to falling costs in the fabrication process, which makes them interesting candidates for large-scale, low-cost applications [1], [2]. The OSC is treated like a crystalline semiconductor where the hopping transport is accounted for by a very low mobility value. The distance between the highest occupied molecular orbital (HOMO) and the lowest unoccupied molecular orbital (LUMO) is used as the bandgap in the model for the OSC. The transistors under investigation are p-type devices. However, for simplicity, the derivation is conducted for an n-type device and an inversion of the terminal voltages, currents and charges afterwards. In Fig. 1,

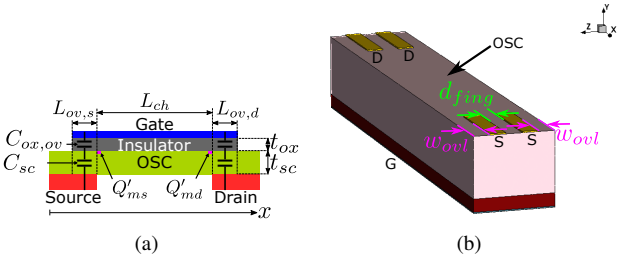

Figure 1. (a) Sketch of the staggered OTFT showing structural parameters and as well capacitances and charge densities. (b) Double-finger OTFT.

a 2D sketch of a staggered organic thin-film transistor and a 3D sketch of a double-finger transistor including some capacitances and structural parameters are shown. Dependent on the applied terminal voltages, a varying amount of charge is accumulated in the channel and in the overlap regions. The overlaps are the regions in which the gate stack overlaps with the source/drain electrodes and their length is denoted as $L_{ov,s}$ and $L_{ov,d}$ in Fig. 1. When the channel current is to be increased, the channel width has to become greater. Due to the fabrication process of the evaporation masks, the channel width cannot be extended beyond certain values. If greater channel widths are desired, the transistor is constructed by several parallel transistors sharing the same gate stack (i. e. the gate electrode, the gate dielectric and the OSC). The drain and source electrodes of each single transistor are then called the fingers. The compact model for the calculation of the charges [3] in single-finger transistors is based on the charge-based DC model presented in [4]. We have presented the extension for multi-finger structures in [5], which will be the topic of this abstract.

This project is funded by the German Federal Ministry of Education and Research ("SOMOFLEX", No. 13FH015IX6) and EU H2020 RISE ("DOMINO", No. 645760), and the German Research Foundation (DFG) under the grants KL 1042/9-2, KL 2223/6-1 and KL 2223/6-2 (SPP FFlexCom). We would like to thank AdMOS GmbH for support. We acknowledge the support by H. Klauk and U. Zschieschang from the Max Planck Institute for Solid State Research, Stuttgart, Germany and as well by M. Seifaei and Y. Manoli from the Fritz Huettinger Chair of Microelectronics, IMTEK, University of Freiburg, Germany.

J. Leise, J. Pruefer, G. Darbandy and A. Kloes are with NanoP, TH Mittelhessen University of Applied Sciences, 35390 Giessen, Germany (e-mail: jakob.simon.leise@ei.thm.de). J. Leise, J. Pruefer and B. Iniguez are with DEEEA, Universitat Rovira i Virgili, Tarragona, Spain.

II. Modeling of the Charges

Observations with Sentaurus TCAD [6] have shown that a remarkable amount of current flows beyond the channel center in the fringing regions. These are the regions between and beyond the fingers. The observations in Fig. 2 show the importance of modeling the fringing regions. The effect of current flowing beyond the channel center is denoted as current spreading, which is schematically shown in a cutplane of the OTFT in Fig. 2(c). The effect of the current spreading is captured in the DC model by introducing an effective channel width $W_{ch,eff}$ which lies between the gate width $W_{ch,G}$ and the actual finger width $W_{ch,SD}$:

$$W_{ch,eff} = \delta_{fit} \cdot (W_{ch,G} - W_{ch,SD}) + W_{ch,SD}, \quad (1)$$

where $\delta_{fit} \in [0,1]$ is a fitting parameter and $W_{ch,G}$ is

$$W_{ch,G} = N_{fing} \cdot W_{ch,SD} + 2 \cdot w_{ovl} + (N_{fing} - 1) \cdot d_{fing}, \quad (2)$$

with N_{fing} as the number of fingers and d_{fing} as the distance between the fingers. The compact DC model equation from [4] is then modified by using $W_{ch,eff}$ instead of simply W_{ch} and the charge equations presented in [3] use the gate width $W_{ch,G}$, since charges are accumulated equally at each z-position (see Fig. 2). The final equations are not shown here for the sake of reducing space. The reader is kindly asked to refer to [5] for further information. The interesting fact is

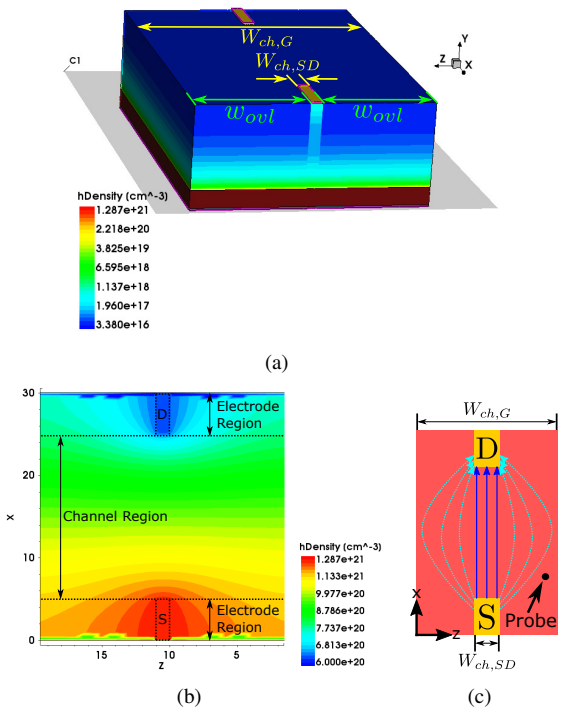

Figure 2. TCAD Sentaurus simulation of a single-finger OTFT with fringing regions. $V_{gs} = -4\,\mathrm{V}$, $V_{ds} = -1\,\mathrm{V}$. (a) shows a 3D sketch of the transistor (not to scale) and (b) shows a cutplane in the OSC directly at the interface between the gate dielectric and the OSC. The color encodes the density of accumulated holes. The color scales are different in (a) and (b). In (b) it can be seen that in the channel region the density of holes is nearly independent on the z-position, whereas in the electrode region it depends on the z-position to a certain degree. As a consequence, charges are accumulated even beyond the channel center in the fringing regions and further paths for the current are opened. In (c) the current spreading in the cutplane is schematically shown. S and D are the projections of the source/drain electrodes. The current flows not only in the channel center (solid arrows) but also in the fringing regions (dotted arrows). At the probe point, the current density is low, but the density of accumulated charges is the same as in the center of the channel.

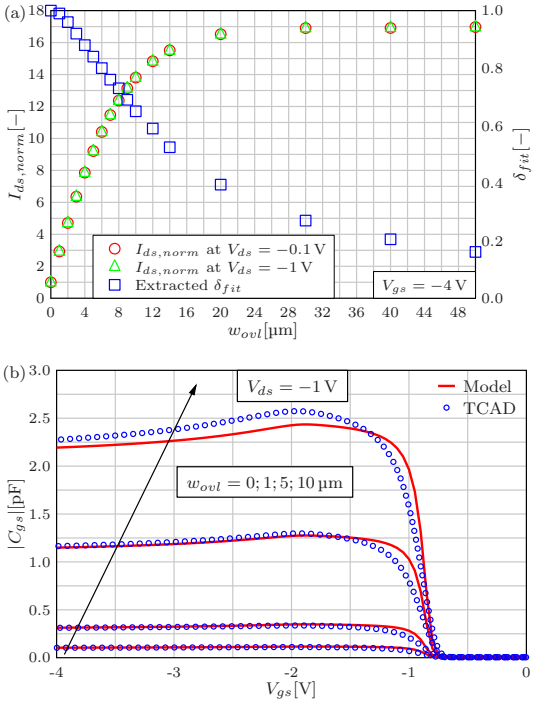

Figure 3. (a) Simulated drain current of a single-finger OTFT at the bias point $V_{gs} = -4\,\mathrm{V}$ for different fringing lengths w_{ovl} for $V_{ds} = -0.1\,\mathrm{V}$ (red circles) and $V_{ds} = -1\,\mathrm{V}$ (green triangles). The drain current is normalized with respect to the current of a transistor without fringing regions ($w_{ovl} = 0$) for both drain voltages. The extracted values for δ_{fit} are shown in blue squares. The transistor parameters are: $L_{ov,s} = L_{ov,d} = 5\,\mu\mathrm{m}$, $L_{ch} = 20\,\mu\mathrm{m}$, $t_{ox} = 5.3\,\mathrm{nm}$, $W_{ch,SD} = 1\,\mu\mathrm{m}$, $\mu_p = 1\,\mathrm{cm}^2\,\mathrm{V}^{-1}\,\mathrm{s}^{-1}$. In the compact model, the mobility is set to $\kappa = 0.93\,\mathrm{cm}^2\,\mathrm{V}^{-1}\,\mathrm{s}^{-1}$ with $\beta = 0$. (b) TCAD simulation of the capacitance C_{gs} of a single-finger OTFT (blue circles) with different fringing lengths w_{ovl} compared to compact model curves (red solid lines) for $V_{ds} = -1\,\mathrm{V}$.

that the fitting parameter δ_{fit} which is necessary to capture the current spreading in the DC model is canceled out in the charge equations.

III. Verification

The model is compared against Sentaurus TCAD 3D simulation results for varying fringing lenthgs w_{ovl}. For each simulation, the fitting parameter δ_{fit} has been determined manually. In Fig. 3(a) the extracted values for δ_{fit} are shown at the example of a single-finger device with different fringing lengths. It can be seen that the value of δ_{fit} is independent on the drain voltage V_{ds}. Even if the value of δ_{fit} does not influence the charge model, a value has to be provided to execute the compact model. Thus, for the verification of the charge model including fringing regions, the values according to Fig. 3(a) are used. As it can be seen in Fig. 3(b), a good agreement of the capacitance C_{gs} between compact model and TCAD simulation can be achieved.

IV. Conclusion

We have presented an extension for a charge-based DC and AC compact model to account for fringing effects in staggered OTFTs. Single-finger devices and multi-finger devices with fringing regions beyond the electrodes and between the fingers are modeled correctly, which has been proven by TCAD simulations for a single-finger OTFT with different fringing region lengths.

References

[1] J. E. Anthony, "Functionalized acenes and heteroacenes for organic electronics," *Chemical Reviews*, vol. 106, no. 12, pp. 5028–5048, 2006, pMID: 17165682.

[2] O. Marinov and M. J. Deen, "Quasistatic compact modelling of organic thin-film transistors," *Organic Electronics*, vol. 14, no. 1, pp. 295 – 311, 2013.

[3] J. Leise, J. Pruefer, G. Darbandy, and A. Kloes, "Charge-based compact modeling of capacitances in staggered otfts," in *2019 Latin American Electron Devices Conference (LAEDC)*, vol. 1, Feb 2019, pp. 1–4.

[4] F. Hain, M. Graef, B. Iñíguez, and A. Klös, "Charge based, continuous compact model for the channel current in organic thin-film transistors for all regions of operation," *Solid-State Electronics*, vol. 133, pp. 17 – 24, 2017.

[5] J. Leise, J. Pruefer, G. Darbandy, M. Seifaei, Y. Manoli, H. Klauk, U. Zschieschang, B. Iniguez, and A. Kloes, "Charge-based compact modeling of capacitances in staggered multi-finger otfts," *IEEE Journal of the Electron Devices Society*, pp. 1–1, 2020.

[6] Synopsys Inc., *TCAD Sentaurus™ Device User Guide*, 2018, Version O-2018.06.

Comparison of WKB and Wavelet Approximations to Determine the Direct Source-to-Drain Tunneling Current in DG MOSFETs

Kerim Yılmaz, Atieh Farokhnejad, Francisco Criado, Benjamín Iñíguez, François Lime and Alexander Kloes

***Abstract*—In this work, a new approach to determine the effect of direct source-to-drain tunneling (DSDT) on 2-D double-gate (DG) MOSFETs is presented. The tunneling probability of electrons with different energy levels and tunneling distances through the potential barrier is calculated using harmonic wavelets and the results are compared to those calculated with the Wentzel-Kramers-Brillouin (WKB) method. Next, by having the tunneling probability the DSDT current is calculated and compared to TCAD simulations data, which are based on WKB model, and also to NanoMOS, a Non-Equilibrium Green's Function (NEGF) 2-D simulator for DG devices.**

***Index Terms*—direct source-to-drain tunneling, Wavelet, WKB, NEGF, Tsu-Esaki formula, tunneling probability, device simulation, double-gate (DG), ultra-short channel, ultra-thin body, short-channel effect (SCE)**

I. Introduction

The degradation of the subthreshold slope S_{sth} and the drain-induced barrier lowering (DIBL) are one of the most frequently discussed aspects of SCEs. Once the device dimensions reach the single-digit nanometer region, the quantum mechanical effects can usually no longer be ignored. This work focuses on DSDT and its influence on the aforementioned SCEs and neglects quantum confinement from gate to gate.
Fig. 1(a) shows the geometry of the studied n-MOS DG transistor. In order to determine the tunneling coefficient of a wave function, it is necessary to solve the time-independent Schrödinger equation. There is no exact solution for potential forms as in the channel of a DG transistor (see Fig. 1(b)). The WKB and the wavelet methods are techniques to obtain approximated solutions for the time-independent Schrödinger equation in 1-D. The WKB approximation is one of the most frequently used methods, but its accuracy is doubtful, as it can only be applied if the potential varies "slowly". The wavelet method is not as fast and easy to implement as the WKB method, but it does not have the mentioned weak points and can therefore be used for various potential forms. It was successfully used, among others, to determine the tunneling coefficient for triangular barriers in MIM (metal-insulator-metal) stack [1] or to compare it with the exact solution of the Schrödinger equation for rectangular barriers [2].

Kerim Yılmaz and Atieh Farokhnejad are with NanoP, TH Mittelhessen - University of Applied Sciences, Giessen, Germany and also DEEEA, Universitat Rovira i Virgili, Tarragona, Spain. F. De Asis Criado López and Alexander Kloes are with NanoP, THM. Benjamín Iñíguez, François Lime are with DEEEA, Universitat Rovira i Virgili. Email: kerim.yilmaz@ei.thm.de

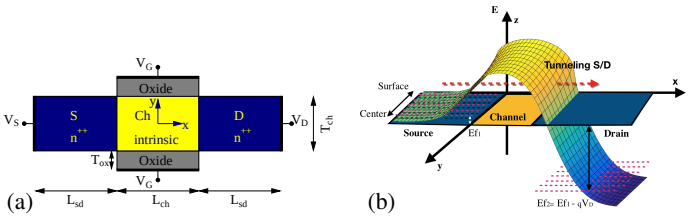

Figure 1. (a) Sketch of the DG MOSFET under study. (b) Illustration of DSDT: Half DG structure superposed with the conduction band edge E_C.

II. Modeling Approach

The first step is to determine the tunneling probabilities for each electron energy and each parallel slice in y-direction of the channel. The used formulas are introduced in the following subsection. For further details please refer to the references.

A. WKB-Based Model

According to the WKB method, the tunneling probability in x-direction is given as [3]:

$$T = \exp\left[-2\int_{x_L}^{x_R} k(x)dx\right] \text{ with } k(x) = \sqrt{\frac{m_{\text{eff}}(V-E)}{\hbar^2/2}}. \quad (1)$$

x_L, x_R are the classical turning points for electrons.

B. Wavelet-Based Model

In wavelet method, it is considered that the solution Ψ of the time independent Schrödinger equation is a superposition of Shannon wavelets. The central point of this method is that by using Shannon wavelets the Schrödinger equation is solved approximately as rectangular potential for each electron energy separately. For this purpose, the wavenumber k(x) is transformed into an equivalent but constant value k_{eq} [2].

$$k_{\text{eq}}^2 = \frac{1}{2\pi}\int_{-2\pi/L_t}^{2\pi/L_t} \hat{K}(\omega)\, d\omega \quad (2)$$

$\hat{K}(\omega)$ is the Fourier transformation of $K(x) = (k(x))^2$ and L_t the tunneling length. The transmission coefficient is part of the calculated wave function outside the barrier and is used for further current calculation.

C. Tunneling Current Density

The net electron tunneling current density along the x-axis is calculated with the TSU-ESAKI tunneling formula [4]

$$J(y) = \frac{q\, m_{\text{eff}}}{2\pi^2\,\hbar^3}\int_{E_{x,\min}}^{E_{x,\max}} T(E_x)\; N(E_x)\; dE_x, \quad (3)$$

with $N(E_x)$ the supply function defined by [5], which is a description of the supply of charge carriers for tunneling:

$$N\left(E_x\right) = k_B\, T\, \ln\left(\frac{1+\exp\left(-\frac{E_C+E_x-E_{f,1}}{k_B\, T}\right)}{1+\exp\left(-\frac{E_C+E_x-E_{f,2}}{k_B\, T}\right)}\right), \qquad (4)$$

where $E_{f,1}$ and $E_{f,2}$ are the Fermi energies at the S/Ch and Ch/D interfaces and E_C is the conduction band edge.

D. Tunneling Current

The calculation of J(y) must be done for each slice along the y-axis. An integration over the mesh size in y-direction and a final multiplication with the channel width W_{ch} gives the total tunneling current through the potential barrier.

$$I_{DS} = W_{ch} \cdot \int_{y_{min}}^{y_{max}} J\left(y\right)\, dy \qquad (5)$$

III. Model Verification and Conclusions

The 2-D potential V(x,y) was extracted from TCAD Sentaurus simulation data [6] to verify the approach simultaneously with the WKB-based model. In order to claim that the wavelet method is better than the WKB approximation the results are also compared to NanoMOS [7], a non-equilibrium Green's Function (NEGF) 2-D simulator for DG MOSFETs with quantum transport model. The NEGF formalism is expected to give more accurate results compared to the WKB method.

Fig. 2 shows that for each electron energy the tunneling probability determined by the wavelet method is always smaller. Thus it can be expected that not only the tunneling current but also the subthreshold swing will be significantly smaller. The question arises as to what influence we expect on the classical DIBL, which we can read from this graph at 100% tunneling probability. The graph in logarithmic scale shows that each electron energy has its own value for the DIBL. The reason for this quasi DIBL is that applying a drain voltage to short-channel transistors not only reduces the height of the potential barrier, but also makes the barrier thinner. This shortens the tunnel length and thus effectively increases the tunneling probability compared to smaller drain voltages. In order to make a statement about where the quasi DIBL visible in the I/V characteristics can be read, its weighting in the energy scale must be taken into account.

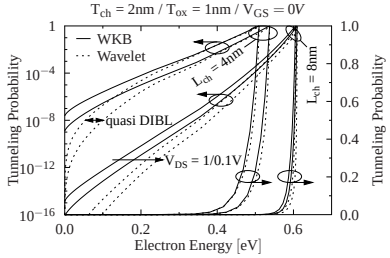

Figure 2. Tunneling probability vs. electron energy in linear and log scale for a short and relatively long channel device.

The weighting is determined by multiplying the tunneling probability with the supply function according to equation (4). This is proportional to the first derivation of the tunneling current density, which we plot against the tunneling probability in Fig. 3(a) for 4nm channel length. As expected the values determined with the wavelet method are smaller than with the WKB method. The interesting aspect of this graph is that the electrons with a tunneling probability of about 10^{-5} respectively 10^{-6} make the largest contribution to the tunneling current because of the Fermi-Dirac distribution. This graph together with Fig. 2 shows that the quasi DIBL is only an average value and cannot be read exactly from the Fig. 2.
Fig. 3(b) shows the normalized first derivation of the tunneling current density vs. the tunneling probability for different channel lengths. With increasing channel length, the peak shifts to higher tunneling probabilities and thus to higher electron energies. A decisive factor for longer channels is the effective tunneling length, which is short enough only for electrons with higher energy. The current disappears with the area under the curve beyond 8 nm channel length.

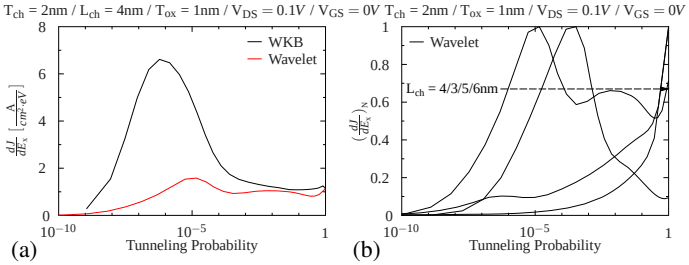

Figure 3. (a) First derivation of the J after E_x vs. tunneling probability. (b) Normalized derivation of J after E_x vs. tunneling probability for different L_{ch}.

In Fig. 4(a) and 4(b) we see a very good agreement of DIBL and S_{sth} for different channel lengths between our wavelet method and NanoMOS simulation data (NEGF-based method). Both are between the results of TCAD simulation data with only drift-diffusion current and only DSDT current. At the same time we have verified that the used WKB method combined with the Tsu-Esaki formula gives similar results as that of TCAD Sentaurus, which uses a WKB-based model.

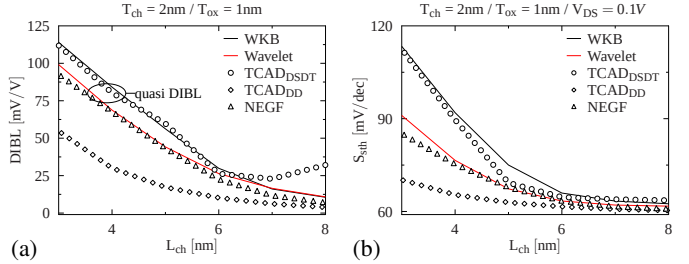

Figure 4. Comparison of DIBL (a) and S_{sth} (b) between wavelet and WKB method, TCAD simulations with only DSDT or drift-diffusion (DD) current and NEGF 2-D simulator with NanoMOS.

References

[1] E.-S. Malureanu, *Univ. Politeh. Buchar. Sci. Bull. Ser. A*, vol. 76, no. 2, pp. 251–262, 2014.

[2] A. Farokhnejad, M. Graef, and A. Kloes, in *Proc. 22nd Int. Conf. Mixed Design of Integrated Circuits Systems (MIXDES)*, Jun. 2015, pp. 210–215.

[3] D. J. Griffiths, *Introduction to Quantum Mechanics*. Prentice Hall, 1995, ch. The WKB Approximation, pp. 274–297.

[4] R. Tsu and L. Esaki, *APL*, vol. 22, no. 11, pp. 562–564, 1973.

[5] A. Gehring, "Simulation of tunneling in semiconductor devices," Ph.D. dissertation, 2003.

[6] Synopsys Inc., *TCAD Sentaurus™ Device UG*, 2018, Version O-2018.06.

[7] Z. Ren, S. Goasguen, A. Matsudaira, S. S. Ahmed, K. Cantley, Y. Liu, Y. Gao, X. Wang, and M. Lundstrom, "NanoMOS," 2016.

Exposure to Thirdhand Smoke induces developmental and metabolic changes in zebrafish embryos

Carla Merino[1], Maria Lorena Cordero-Maldonado[2], Emma L. Schymanski[3], Xavier Correig[1], Maria Vinaixa[1], Noelia Ramírez[1]

1. Metabolomics Interdisciplinary Lab, Department of Electrical Electronic Engineering and Automation, University Rovira i Virgili, Institute for Health Investigation Pere Virgili, CIBERDEM, 2. Aquatic Platform, Luxembourg Centre for Systems Biomedicine (LCSB), University of Luxembourg 3. Environmental Cheminformatics Group, LCSB, University of Luxembourg.

E-mail contact: carlamelissa.merino@urv.cat

1. Introduction

Tobacco smoke, formed by a complex mixture of particles and thousands of toxicants including over 70 carcinogens according to the International Agency for Research on Cancer [1], is a ubiquitous outdoor and indoor environmental pollutant that has been overlooked to date by the environmental and health policies. Most of the smoke gases and particles deposit, age and remain for long periods of time in fabrics, surfaces and dust forming the so-called **thirdhand smoke** (THS), a less studied source of exposure to tobacco smoke toxicants that especially affects children living with smokers. THS components not only remain on surfaces and in settled dust, but they can also be re-emitted into the gas phase or even react with oxidants and other atmospheric compounds to yield secondary contaminants, some of them with increased toxicity [2]. This is the case of nicotine, which reacts to form tobacco-specific nitrosamines (TSNAs), a leading class of highly mutagenic and carcinogenic compounds in tobacco products [3]. House dust is a repository of contaminants and an important route of toxicant exposure, especially for children under 5-year-old, who spend most of their time indoors and are estimated to ingest about 100 mg of indoor dust per day [4]. One of the first studies on THS pollution estimated the cancer risk related to carcinogen N-nitrosamines and TSNAs in THS by dermal absorption and involuntary ingestion of settled house dust from smokers' and non-smokers' homes [5]. The results revealed that the estimated lifetime cancer risk associated to THS exposure in children from 1 to <6 years old was higher than the United States Environmental Protection Agency (USEPA) and the World Health Organization (WHO) recommendations in all smokers' homes and in most of the non-smokers' ones. This showed strong evidence of THS health risk and demonstrated the ubiquitous presence of tobacco smoke pollutants. Despite this evidence, the THS toxicity and the related health effects observed in cells and murine models [6] to date, few studies characterize the phenotypic and metabolic alterations induced by THS exposure in early development.

2. Objective

The aim of this study is to test the effects of THS toxicants exposure in early development. To accomplish this, we exposed zebrafish embryos to THS toxicant mixtures, mimicking the exposure concentrations of children living in smokers' and non-smokers' homes. The alterations caused by this exposure were evaluated by developmental observation of zebrafish embryos combined with untargeted metabolomics and lipidomics.

3. Materials and methods

3.1. Zebrafish exposure

Embryos of wildtype (AB) zebrafish line, obtained by natural mating, were incubated with THS toxicants (nicotine and TSNAs) from two starting points, 6 hours post fertilization (hpf) and 24 hpf, till 120 hpf. As shown in Table 1, we performed two tests: *1) zebrafish embryos exposed to THS toxicants at different concentration ranges, according with our previous results in non-smoker's and smoker's house dust; and 2) embryos exposed to concentrations that mimic the exposure of young children in smokers' and non-smokers' homes.* Non-treated controls were processed in parallel by exposing the embryos to the vehicle only (0.3X Danieau's medium). All incubations were performed in five technical replicates.

Table 1. Exposure concentrations of THS toxicants for test 1 and 2

	Test 1				Test 2				
	T1-Ctrl	**T1-Con1**	**T1-Con2**	**T1-Con3**	**T2-Ctrl**	**T2-Con1**	**T2-Con2**	**T2-Con3**	**T2-Con4**
Nicotine	0 µM	31 µM	308 µM	3084 µM	0 µM	1 µM	6 µM	31 µM	62 µM
TSNAs	0 µM	0.1 µM	1 µM	10 µM	0 µM	$2x10^{-3}$ µM	$2x10^{-2}$ µM	0.1 µM	0.2 µM

Ctrl: Control group; Con: Concentration

Phenotypic development of embryos was followed daily during the exposure and the anatomical changes were noted. Further, *fli1*:EGFP zebrafish embryos were also used during Test 1 for the study of blood vessel development. For the second test, pools of zebrafish embryos were gathered for each biological replicate, snap-frozen in dry ice and stored at -80 °C until sample extraction for metabolomics and lipidomics analysis.

3.2. Metabolic and lipidomic sample extraction

The collected embryos were extracted by dual phase extraction with dichloromethane, methanol and water to separate the polar (methanol:water) and the non-polar (dichloromethane) fraction. Additionally, the non-polar fraction was dried and reconstituted in methanol:toluene. Quality control samples (QCs) of polar and non-polar fraction were prepared by pooling equal volumes of each sample, respectively. Samples and QCs were stored at -80 °C until LC-MS analysis.

3.3. Untargeted LC-MS analysis and data processing

Samples were analysed by UHPLC-HRMS using a Thermo Ultimate 3000 LC - Thermo QExactive. Metabolites and lipids from polar and non-polar fraction, respectively, were separated in normal and reverse phase modes. Several QCs were injected before the first sample and then repeatedly analysed throughout the sequence. Following data acquisition and processing, univariate and multivariate statistical analysis was performed to differentiate the significant features. Metabolites and lipid identification were done using reference standards and advanced data identification tools.

4. Results and discussion

4.1. Phenotypic response of zebrafish embryos to THS toxicants at 120 hpf

As showed in Figure 1B, the highest concentration (T1-Con3) of THS toxicants resulted in total lethality, indicating the high toxicity to the embryos. Zebrafish embryos exposed to the previous concentration (T1-Con2) showed increased occurrence of severe phenotype (Figure 1A), developing oedemas and spine curvature, and more than the 50% of lethality. Moreover, no observational differences were found between the lowest concentration (T1-Con1) and the control group. Similar results were found for all the concentrations of Test 2 (figure not shown) where concentrations were adapted to childhood dust ingestion. No differences were observed between 6 hpf and 24 hpf starting points.

Further, the exposure of *fli1*:EGFP zebrafish embryos did not show significant differences in the development of blood vessels.

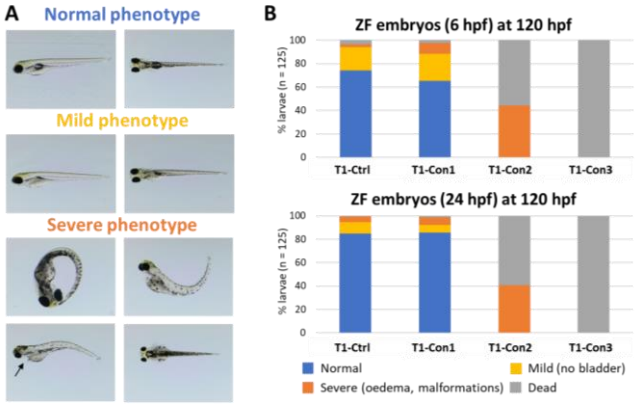

Figure 1. Phenotypical observation of zebrafish embryos from Test 1 exposed to THS toxicants at 120 hpf. (A) Morphological changes in different categories; (B) Percentage of embryos at each category per group.

4.2. Metabolomics of THS exposure

More than 150 features in polar fraction were dysregulated due to THS exposure. Several nicotine (Figure 2) and TSNAS metabolites were found upregulated in the exposed groups. As expected, higher concentrations of THS toxicants resulted in higher intensity of exposure metabolites. Different endogenous metabolites and metabolic pathways were also altered in embryos exposed to THS toxicants.

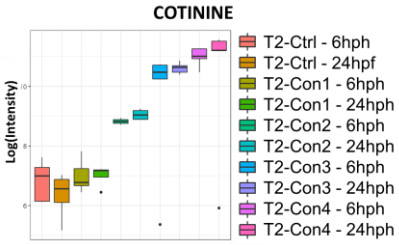

Figure 2. Box plot of the main nicotine metabolite, cotinine, found in zebrafish exposed to non-smoker's and smoker's house dust adjusted to children dust ingestion.

4.3. Lipidomics of THS exposure

Lipidomics analysis revealed differences in the lipid pattern. As shown in Figure 3, the PLS-DA of 5482 non-polar features for the 6 hpf starting point revealed that zebrafish embryos exposed at different concentrations of THS toxicants are notably separated from the control group, mostly in a concentration-dependent manner, confirming the results seen in the metabolomic analysis. Similar effects were found for the 24 hpf starting point.

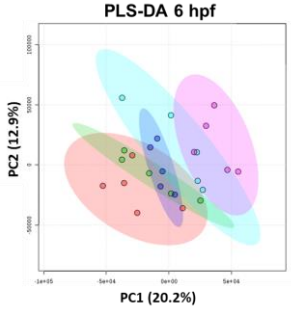

Figure 3. Partial least-squares discriminant analysis (PLS-DA) of features found in non-polar fraction of zebrafish exposed to THS toxicants for 6 hpf starting point.

● *T2-Ctrl;* ● *T2-Con1;* ● *T2-Con2;* ● *T2-Con3;* ● *T2-Con4.*

5. Conclusions

The results summarized here demonstrate that exposure to THS affects early development, generating phenotypic and metabolic alterations. In order to validate these results, future work will focus on the effects of exposure to THS extract samples.

6. References

[1] IARC Monograph Vol. 83. Tobacco Smoke and Involuntary Smoking; 2004.
[2] Matt, G. *et al*. Environmental Health Perspectives. 2011 Sep; 119(9): 1218–1226.
[3] WHO. Tobacco and its environmental impact: an overview; 2017.
[4] Ott, W. E. *et al*. Exposure Analysis. CRC Press; 2006.
[5] Ramirez, N. *et al*. Environment International 2014, 71 (0), 139-147.
[6] Hang B. *et al*. International Journal of Molecular Sciences 2017, 18, 932.

Acknowledgements – The authors want to acknowledge the financial support of Direcció General de Recerca of the Government of Catalonia (2019FI_B1 00159); European Commission (H2020-MSCA-IF-2014-660034); and the Spanish Ministry of Economy (IJCI-2015-23158 & TEC2015-69076-P). ELS is supported by the Luxembourg National Research Fund (FNR) for project A18/BM/12341006.

Design and implementation of a parametrizable and scalable ADC on a FPGA for switched mode power supply.

Juan David Espitia, Enric Vidal Idiarte, Enric Cantó Navarro

Automatic Control and Industrial Electronics Group (GAEI). Universitat Rovira I Virgili. Avinguda dels Paisos Catalans, 26 Tarragona-Spain
Email: juandavid.espitia@urv.cat

Abstract

The aim of this work is the design and implementation of a modular ADC in a FPGA. Taking advantage of the versatility of the FPGA, the design can be adapted to the application requirement. The design is implemented using very high-speed integrated circuit hardware description (VHDL). Two ADC topologies are presented, the ADC based on the one-shot circuit and ADC based on SAR (Successive approximation register), with a minimum number of external analog components used.
Keywords: FPGA, VHDL, SAR, One-Shot

1. Introduction

Analog-to-digital converter (ADC) are widely used in the control system industry, is one of the most critical stages of the process. The traditional method for analog to digital conversion is made by a dedicated ADC chip. The ADC is used primarily in the feedback loop. It can, however, be part of the self-calibrating process. Its sampling rate and resolution are important parameters and its accuracy influences the performance of the overall process.

The FPGA are built from the join of lookup table ("LUT"), multiplexers, flip-flop etc. The LUT can implement any logic function. Each LUT can be connected to other one through interconnect resources. Complex design can be implemented connecting a high number of LUT.

The ADC is not integrated on the FPGA, the ADC must be implemented externally. Although using external ADC solve the analog interface problem, it increases the total cost of the design.

The implementation of the ADC in a FPGA is more desirable due to the reduced cost, space and components since it does no rely on any external ADC converter [1]. Also, the advantage of implementing several ADC based on FPGA in case of managing more than one signal. Design a custom-made ADC leads to flexibility in choosing the sampling rate and resolution. The ADC can be accomplished by using digital input and output.

2. ADC based on One-Shot circuit

One of the topologies presented in this work is the ADC based on One-Shot circuit. The aim of this technique is to take advantage of the charge and discharge process of a capacitor [2]. The One-shot circuit shown in Fig.1. is made with a NOT and NOR gate, one resistor and a capacitor.

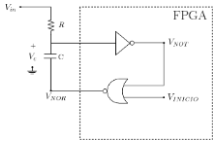

Fig.1. One-shot circuit implementation

Under the steady-state conditions, $V_{Trigger}$ is low and the output of the NOR (V_{NOR}) is high, thus the voltage V_C is pulled high through the resistor R up to the sampled signal level. The output of the NOT (V_{NOT}) gate is low. Once $V_{Trigger}$ is high, V_{NOR} is low and V_{NOT} goes to high. Due to the feedback between V_{NOT} and the NOR gate input, the NOR holds V_{NOR} low. After $V_{Trigger}$ is high, the capacitor voltage (V_C) begin to charge through R, until V_C reach the NOT gate threshold voltage (V_{th}), changing V_{NOT} to low and V_{NOR} high. The length (T_{in}) of V_{NOT} while is high, is what the FPGA measure. The one-shot circuit generates an output pulse that its duration es inversely proportional to the amplitude of sampled signal (V_{in}). The relation between T_{in} and V_{in} can be expressed at the Eq. 1, where ΔV_O is the FPGA logic voltage. The behavior of V_c and V_{NOT} is shown in the Fig.2. where $V_{in} = 0.5\ V$ and $V_{in} = 0\ V$.

$$T_{in} = RC \cdot \ln\left(\frac{\Delta V_O}{V_{in} - V_{th}}\right) \qquad (1)$$

A counter is implemented to obtain T_{in} duration. Once T_{in} is obtain, V_{in} can be found based on the Eq. 1. The ADC based on the one-shot circuit resolution, depends on the FPGA clock frequency. While V_{NOT} is high, the counter increases the count register by 1 in every rising

edge of the clock. In [3] is implemented a counter using rising and falling edge, increasing the counter frequency by two. The V_{in} range is limited to V_{th}. A voltage (V_{sum}) is added to increase V_{in} range, modifying Eq.1.

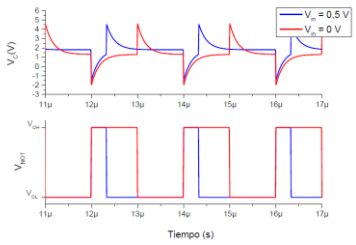

Fig.2. V_c and V_{NOT} with different V_{in}

3. ADC based on SAR

Another topology is presented in this work. The ADC based in SAR is composed of a DAC, SAR logic and a comparator. Using the DAC, the SAR logic search through all the possible quantization levels before reaching to the digital output (B). To implement the DAC in the FPGA is needed N number of outputs. In [4] the DAC is replaced with a pulse width modulator (PWM) and a low pass filter (LPF).

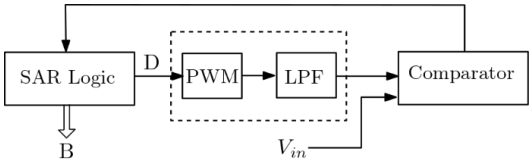

Fig.3. Schematic ADC based on SAR

Replace DAC with PWM and LPF is supported by the fact that a DC level can be achieve after low passing a PWM signal. The LPF output is DC voltage with a ripple. Varying the dutty cycle (D), any DC level can be obtained from a PWM and LPF. By low passing the PWM the even harmonics are removed.

The ADC resolution is given by the PWM number of bits (N). To achieve the resolution the ripple needs to be less than an LSB ($\frac{\Delta V_O}{2^N}$), so the LPF must be modified. Decreasing the cut-off frequency (f_c) respect to the PWM frequency (f_{PWM}), decrease the ripple, but the settling time of the LPF is slower. On the other hand, if the f_c is higher the ripple increase but the settling time is faster. It needs to be chosen an f_c low enough that the ripple is lower than an LSB, but high enough to get a settling time high. The order of the LPF also affect the dynamic of the time response. The ripple decreases when the order increases, but the settling time is slower, also the implementation is more expensive. On the other hand, the ripple increases when the order is lower, but the settling time is faster.

4. Experimental results

Experiments are carried out for an 8-bit ADC based on SAR, replacing the DAC for a PWM and LPF. It was implemented with the values shown in the Table.1.

LPF order	PWM frequency	Settling time LPF	Conversion time	Sample frequency
3	781 KHz	15 μs	120 μs	8.33 KSPS

Table 1 Value implemented for 8 bits ADC

Using a triangular signal of V_{in} with frequency of 16.275 Hz. To check the conversion result (B) an external DAC is implemented. Once B is obtained is sent to the DAC. The blue signal es B, where it can be seen is move due to the conversion time.

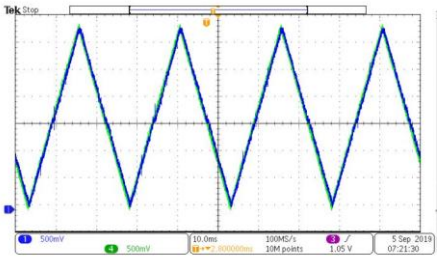

Figure 4 V_{in} and B for 8-bit ADC

5. Conclusions

Two topologies for ADC are presented, An ADC based on SAR, replacing the DAC for a PWM and LPF is implemented. This modification reduces the number of outputs use by the FPGA. This topology is implemented with an external LPF. The second topology implement an ADC based on the one-shot circuit. Based on the length of V_{NOT}, V_{in} can be obtain. This topology is implemented with minimum of extra analog devices. Both topologies are scalable and parametrizable for a different ADC resolution.

References

[1] M. Ummaruddin, G. M. Phade, S. T. Gandhe and P. A. Dhulekar, "Implementation of FPGA Based Digital Camera System Controlled from an LCD Touch Panel," *2015 International Conference on Computing Communication Control and Automation*, Pune, 2015, pp. 949-954, doi: 10.1109/ICCUBEA.2015.188.

[2] E. Abramov, T. Vekslender, O. Kirshenboim and M. M. Peretz, "Fully Integrated Digital Average Current-Mode Control Voltage Regulator Module IC," in *IEEE Journal of Emerging and Selected Topics in Power Electronics*, vol. 6, no. 2, pp. 485-499, June 2018, doi: 10.1109/JESTPE.2017.2771949.

[3] Z. Lukic, N. Rahman and A. Prodie, "Multibit Sigma–Delta PWM Digital Controller IC for DC–DC Converters Operating at Switching Frequencies Beyond 10 MHz," in *IEEE Transactions on Power Electronics*, vol. 22, no. 5, pp. 1693-1707, Sept. 2007, doi: 10.1109/TPEL.2007.904199.

[4] G. D. Colletta, L. H. C. Ferreira, T. C. Pimenta and P. C. Crepaldi, "A Successive Approximation A/D Converter Using a PWM Modulator DAC," *2012 IEEE Ninth Electronics, Robotics and Automotive Mechanics Conference*, Cuernavaca, 2012, pp. 333-337, doi: 10.1109/CERMA.2012.59.

Gold Nanoparticle-Assisted Black Silicon Substrates for Mass Spectrometry Imaging Applications

Stefania Alexandra Iakab†‡, Pere Ràfols†, Xavier Correig†‡§, María García-Altares†‡

†Department of Electronic Engineering, Rovira i Virgili University, Tarragona, 43007, Spain
‡Spanish Biomedical Research Centre in Diabetes and Associated Metabolic Disorders (CIBERDEM), Madrid, 28029, Spain
§Institut d'Investigacio Sanitària Pere Virgili, 43204, Tarragona, Spain

Abstract

Gold-coated black silicon serves as an exceptional substrate for Surface Assisted Laser Desorption-Ionization Mass Spectrometry Imaging. It is safe to produce, compatible with current MSI workflows, and suitable for functionalization to selectively analyze molecules transferred to the substrate. Analyses of human fingerprints and mouse tissues illustrate this technology.

1. Introduction

Matrix-free mass spectrometry imaging (MSI) technologies are gaining popularity for detecting low molecular mass compounds from complex biological samples. Silicon based substrates proved their value as desorption/ionization on silicon (DIOS) and nanostructure initiated mass spectrometry (NIMS) substrates, successfully detecting small molecules with reduced background noise and fragmentation, despite their unsafe fabrication method [1] [2]. Alternatively, Au nanoparticles were used in laser desorption ionization MSI analyses with increased resolution and sensitivity [3]. We developed Au coated black silicon substrates (AuBSi) with separate hydrophobic and hydrophilic selective regions for MSI applications on biological tissues.

2. Methods

The BSi substrates were created by dry etching using SF_6 and O_2 plasma mixture [4]. The Au nanolayer was deposited by sputtering and the hydrophobic or hydrophilic surfaces were created with CHF_3 or O_2 plasma, respectively. Substrates were analyzed by SEM, AFM, UV-VIS spectroscopy and mean contact angle. Molecules from human fingerprints were transferred onto the substrate by touching and the animal tissue samples were cryo-sectioned, the slices were placed onto the substrates for 1 minute of interaction between tissue and surface and then removed with abundant water and dried before analysis.

3. Results

Physicochemical characterization of the AuBSi substrates showed an array of silicon nanopillars (~250 nm height) decorated with gold nanoparticles (~10 nm diameter), resembling a forest of nano-asparagus (Figure 1.) that absorbs ~95% of visible light, specifically, 98% at 355 nm (the wavelength of the MALDI Nd:Yag laser). The hydrophobic regions of the substrates have a mean contact angle (CA) >123º, because of the CH terminal groups, while the hydrophilic regions have a mean CA <17º, due to the OH terminal groups. The AuBSi substrates proved efficient for detecting standard compounds from liquids (glucose folic acid and phosphocholine – Figure 2) as well as metabolites from tissue samples. The detected Au cluster peaks allowed an accurate mass calibration process throughout the full mass range.

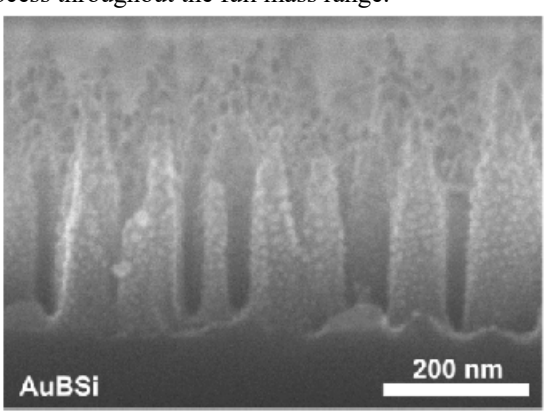

Figure 1. SEM image of the AuBSi nanostructure

Metabolites from sweat glands and sebaceous glands and compounds adhered to fingerprints were detected on the AuBSi using positive and negative ionization modes. We detected several ions in the range m/z 150−900, which could be both endogenous (e.g., fatty acids and lipids) and exogenous compounds (residues from soap or laboratory gloves).

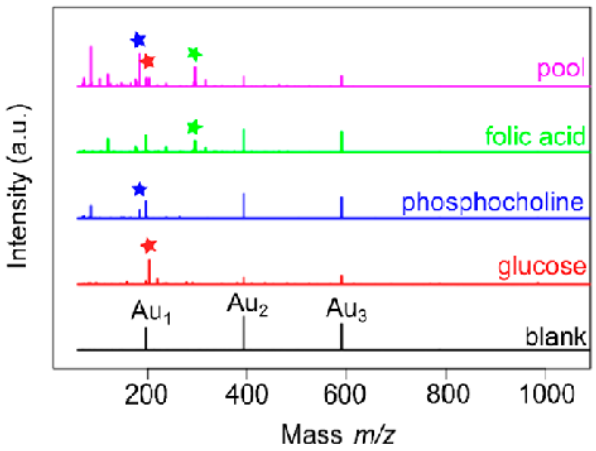

Figure 2. Mass spectra of standard metabolites from liquids deposited onto the AuBSi

We then investigated if our AuBSi surface could be used to monitor exogenous compounds on fingerprints in a targeted manner, such as drug residues from someone who has touched or manipulated a powdered compound. For this example, we attempted to detect the commercial drug paracetamol. Two fingerprints were stamped onto the functionalized AuBSi substrate: one control and one after a volunteer rubbed a paracetamol pill on the second finger. The representative peaks of paracetamol ($[M + Na]^+$ and $[M + K]^+$ cations, m/z 174.04 and m/z 190.01) were detected in the positive mode (Figure 3).

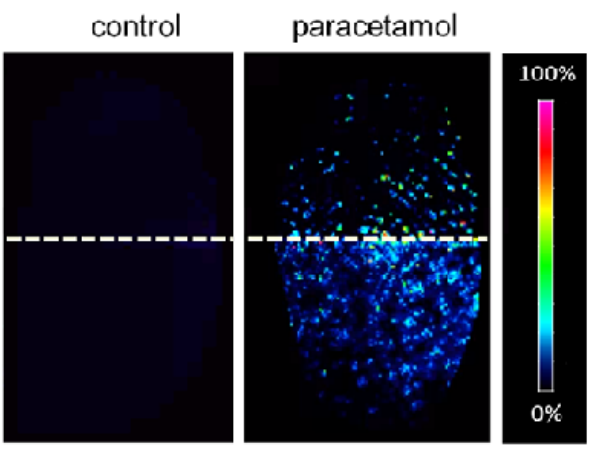

Figure 3. Distribution of sodium adduct of paracetamol on clean and contaminated fingerprint

For analysing animal tissues, fresh frozen kidney and brain tissues were sectioned at 5 µm, and MSI data were acquired in negative mode, because of the greater sensitivity shown in the preliminary measurements. MSI of kidney sections revealed several representative ions of the different morphological regions of the organ, for example, m/z 283.27 is mainly found in the outer medulla region, and ions m/z 778.53 and 906.68 are found in the cortex region. For brain tissue, several ions in the range m/z 800−900 were found in the grey matter of the mouse cerebellum, corpus callosum, fornix, pons, and medulla oblongata (Figure 4).

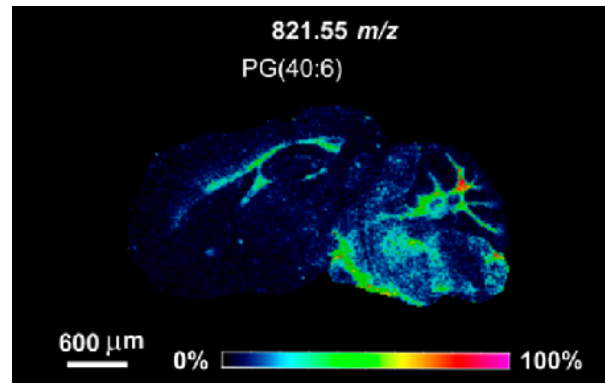

Figure 4. Brain MSI representing the distribution of a brain lipid PG(40:6)

4. Conclusions

We developed a surface on which matrix-free LDI-MS imaging experiments based on BSi decorated with gold can be performed. The surface is produced with a straightforward protocol that is easy to replicate and poses no risk for users. By sputtering gold nanoparticles onto the BSi surfaces, we increased their efficiency as SALDI-MS substrates and enabled detection of metabolites from fingerprints and molecules transferred from animal tissues in both positive and negative ionization modes. With this technique, we acquired high quality images from mouse brain and liver tissues. Moreover, our surfaces can easily be functionalized to selectively monitor compounds in terms of their physicochemical properties. We envisage that versatile substrates based on safe materials like silicon and gold will have a considerable impact as a matrix-free strategy for performing in situ metabolomics on biological samples.

References (Times 10 bold)

[1] Wei, J., *et al. Desorption – ionization mass spectrometry on porous silicon*, Nature, vol. 399, 1999.
[2] Northen, T. R. *et al. Clathrate nanostructures for mass spectrometry*, Nature, vol. 449, 2007.
[3] McDonnell, L. A., *et al., Imaging Mass Spectrometry,* Mass Spectrom. Rev., vol. 26, 2007.
[4] Iakab, S. A., *et al. Gold Nanoparticle-Assisted Black Silicon Substrates for Mass Spectrometry Imaging Applications*, ACS Nano, 2020

Physical Interpretation of the Current Path in Staggered Organic Thin-Film Transistors

Jakob Pruefer[1,2,✠], Jakob Leise[1,2], Ghader Darbandy[1], Aristeidis Nikolaou[1,2], Benjamín Iñíguez[2] and Alexander Kloes[1]

[1]NanoP, TH Mittelhessen University of Applied Sciences, Giessen, Germany,
[2]DEEEA, Universitat Rovira i Virgili, Tarragona, Spain,
✠jakob.pruefer@ei.thm.de

***Abstract*—Already existing compact models [1] for short-channel effects as threshold-voltage roll-off and drain-induced barrier lowering (DIBL) in staggered organic thin-film transistors (TFT) are extended in terms of improving the models in view of the physical interpretation. This work shows that the location of the most leaky path for the source to drain current depends in staggered TFTs on the gate-source voltage and threshold voltage of the transistor. For this, simulation data were obtained with the Technology CAD (TCAD) software Sentaurus. The location of the current path is important for the compact models, since these are defined on the barrier maximum height along it. Thus, a comprehension about the channel location is essential for the extraction of the potential and definition of the compact models. Finally, a charge-based current compact model [2] was fitted to TCAD simulations with the new physical comprehension and interpreted regarding to them.**

I. Introduction

The downsizing of the structural width is a proven approach to increase the influence of the gate-source voltage and the drain-source voltage on the drain current. Electronic circuits with lower supply voltages can be realized, which reduces the power consumption of the whole system. As soon as the reduction in staggered organic TFTs reaches a channel length of less than 1 µm, physical effects such as subthreshold-slope degradation, threshold-voltage roll-off and drain-induced barrier lowering (DIBL) appear [1]. For the derivation and definition of compact models for these effects the potential along the current channel is of essential importance. In the case of an organic TFT with a staggered structure, the charge-carriers do not always flow along the gate-dielectric/semiconductor interface as in coplanar structures. The most leaky path shows a dependence on the gate-source voltage and the threshold voltage.

This work extends the compact models about the threshold-voltage roll-off and drain-induced barrier lowering (DIBL) presented in [1] in terms of improving the models in view of the physical interpretation about the location of the current channel on which the compact models are defined.

This project is funded by the German Federal Ministry of Education and Research ("SOMOFLEX", No. 13FH015IX6) and EU H2020 RISE ("DOMINO", No. 645760), and the German Research Foundation (DFG) under the grants KL 1042/9-2, KL 2223/6-1 and KL 2223/6-2 (SPP FFlexCom). We would like to thank AdMOS GmbH for support. We acknowledge the support by H. Klauk, James W. Borchert and U. Zschieschang from the Max Planck Institute for Solid State Research, Stuttgart, Germany.

II. Channel Location

The path taken in staggered TFTs by the charge-carrier from source to drain depends on the gate-source voltage. Figure 1 shows results from TCAD simulations of a p-type organic TFT and its charge-density distribution along a cutline at the center of the channel. The depth defines the distance between the point of interest along the cutline and the gate electrode. When the organic TFT is operated with a gate-source

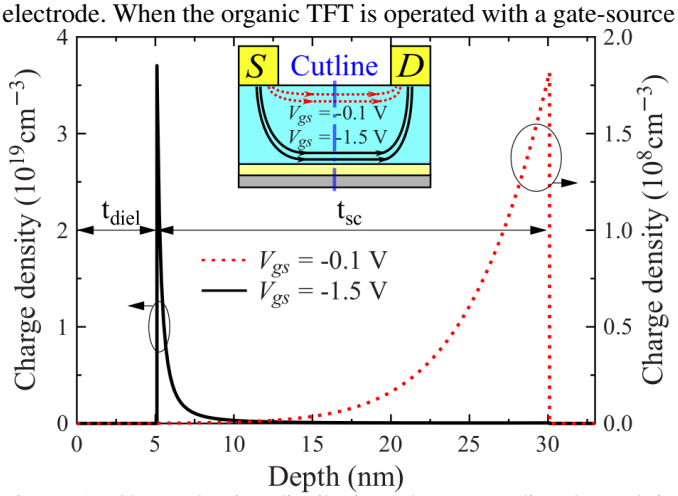

Figure 1: Charge-density distribution along a cutline located in the center of the accumulation channel of a TCAD-simulated p-type organic TFT operated above the threshold voltage (black line; $V_{gs} = -1.5\,\mathrm{V}$) and operated below the threshold voltage (red line; $V_{gs} = -0.1\,\mathrm{V}$). With device parameters: channel length $L_{ch} = 100\,\mathrm{nm}$, semiconductor thickness $t_{sc} = 25\,\mathrm{nm}$ and gate-dielectric thickness $t_{diel} = 5.1\,\mathrm{nm}$.

voltage of $V_{gs} = -1.5\,\mathrm{V}$ (above the threshold voltage), the channel is located close to semiconductor-dielectric surface, as expected [4]. However, when the transistor is operated with a gate-source voltage of $V_{gs} = -0.1\,\mathrm{V}$ (below the threshold voltage), the leakage current flows from source to drain far away from the semiconductor-dielectric surface, equidistant from gate to source/drain contacts. This shows that when defining compact models for short-channel effects, such as threshold-voltage roll-off and DIBL, the extraction of the barrier maximum height must consider the bias conditions of the operation point of the respective short-channel effect.

III. Compact Models of Short-Channel Effects

The work in [1] presents compact models for the short-channel effects threshold-voltage roll-off and DIBL defined on

a potential solution of the two-dimensional potential problem of a staggered structure. Both models depend on the channel length L_{ch}, the semiconductor thickness t_{sc}, the gate-dielectric thickness t_{diel} and the permittivities for the semiconductor ϵ_{sc} and the gate-dielectric ϵ_{diel} [1]:

$$\Delta V_{T,roll-off} = -V_{bi}\frac{4(t_{sc}+t_{diel}\epsilon_{sc}/\epsilon_{diel})d_{poi}}{4(t_{sc}+t_{diel}\epsilon_{sc}/\epsilon_{diel})^2+L_{ch}^2}, \quad (1)$$

$$\Delta V_{DIBL} = V_{ds}\frac{2(t_{sc}+t_{diel}\epsilon_{sc}/\epsilon_{diel})d_{poi}}{4(t_{sc}+t_{diel}\epsilon_{sc}/\epsilon_{diel})^2+L_{ch}^2}, \quad (2)$$

where V_{bi} is the built-in voltage and V_{ds} is the drain-source voltage. Both models include the fitting parameter d_{poi} which defines the distance between the point of interest (channel location) and the gate electrode. The parameters of the TCAD-simulated organic p-type TFTs employed for verification in Fig. 2 and Fig. 3 are: $t_{sc} = 25\,\mathrm{nm}$ and gate-dielectric thickness $t_{diel} = 5.1\,\mathrm{nm}$.

Figure 2 illustrates the threshold-voltage roll-off depending on the channel length from 1 to $0.1\,\mu\mathrm{m}$ calculated using Equation (1) compared to extracted values from transfer characteristics and potential simulated with the TCAD software Sentaurus. The values from transfer characteristics are extracted by g_m/I_d method [3]. In case of the threshold voltage roll-off an emerged accumulation channel is expected. Consequently, the best agreement was obtained for a channel location at gate-dielectric/semiconductor interface and thus $d_{poi} = 5.1\,\mathrm{nm}$. The agreement between the extraction from transfer characteristics and the potential from the same TCAD simulations also confirms the expectations from Fig. 1.

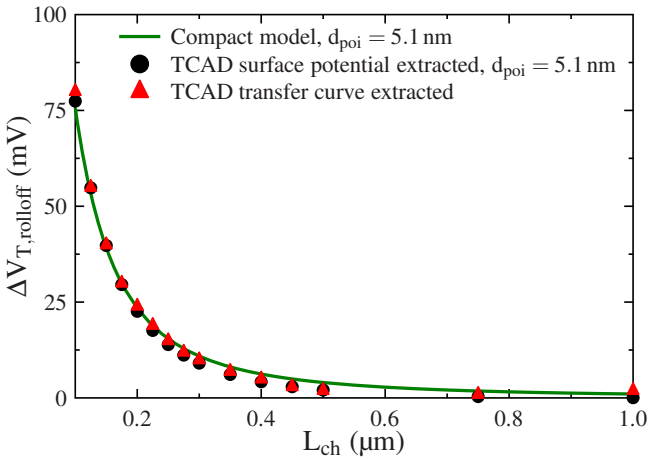

Figure 2: Threshold voltage roll-off depending of the channel length L_{ch} calculated using Equation (1) (Compact model) and compared to TCAD simulations of the surface potential in the channel and of the transfer characteristics. The best agreement was obtained for $d_{poi} = 5.1\,\mathrm{nm}$.

Since the DIBL effect occurs below the threshold voltage, the most leaky path of the current emerges far away from the gate-dielectric/semiconductor interface as illustrated in Fig. 1 in the cross-section (red dotted line). Hence, the best agreement is obtained for $d_{poi} = 29.1\,\mathrm{nm}$ at an entire device thickness of $t_{diel} + t_{sc} = 30.1\,\mathrm{nm}$. Here, the potential profile in the vertical direction (blue dashed line) through the entire device thickness is assumed as linear. This is an approximation that leads to an error with increasing d_{poi}, but the results in Fig 3 show that the effect can be modeled quite precisely. Figure 3 shows the threshold-voltage shift ΔV_{DIBL} caused by the DIBL effect calculated using Equation (2) compared to TCAD-simulated data extracted from transfer characteristics and the potential. Here again, the agreement between the extraction from transfer characteristics and the potential from the same TCAD simulations also confirms the expectations from Fig. 1.

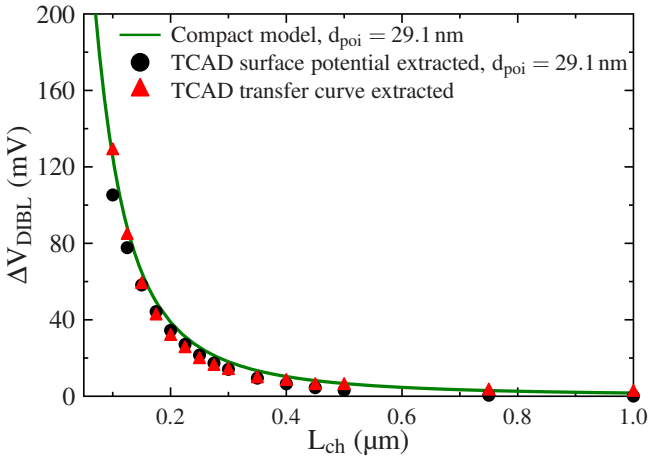

Figure 3: DIBL-induced threshold-voltage shift ΔV_{DIBL} depending of the channel length for $V_{ds} = -1\,\mathrm{V}$ calculated using Equation (2) (Compact model) and compared with TCAD simulations extracted of the surface potential in the channel and of the transfer characteristics. The best agreement was obtained for $d_{poi} = 29.1\,\mathrm{nm}$.

IV. Conclusion

We have presented that the current path from source to drain in staggered TFTs depends on the gate-source voltage and threshold voltage of the transistor. When the thin-film transistor is operated below the threshold voltage, the charge carrier path from source to drain occurs far away from the gate-dielectric/semiconductor interface very close to the source/drain contacts. This is important to consider for the definition of the DIBL compact model. When the transistor is operated above the threshold voltage, an accumulation channel emerges at the gate-dielectric/semiconductor interface and this must be considered for the definition of the threshold-voltage roll-off compact model.

References

[1] J. Prüfer, J. Leise, G. Darbandy, J. W. Borchert, H. Klauk, B. Iñíguez, T. Gneiting and A. Kloes, "Analytical Model for Threshold-Voltage Shift in Submicron Staggered Organic Thin-Film Transistors," *Proc. MIXDES*, Rzeszów, Poland, June 2019.

[2] F. Hain, M. Graef, B. Iñíguez and A. Kloes, "Charge based, continuous compact model for the channel current in organic thin-film transistors for all regions of operation," *Solid-State Electronics*, vol. 133, pp. 17–24, July 2017.

[3] D. Flandre, V. Kilchytska and T. Rudenko , "g_m/I_d Method for Threshold Voltage Extraction Applicable in Advanced MOSFETs With Nonlinear Behavior Above Threshold," *IEEE Electron Device Letters*, Vol. 31, No. 9, pp. 930-932, September 2010.

[4] F. Dinelli, M. Murgia, P. Levy, M. Cavallini, F. Biscarini and D. M. de Leeuw, "Spatially Correlated Charge Transport in Organic Thin Film Transistors," *Phys. Rev. Lett.*, vol. 92, no. 11, Art. no. 116802, March 2004.

Impedance Spectroscopy Analysis of Indoor Organic Solar Cells: A Study Case

Alfonsina Abat Amelenan Torimtubun, Josep Pallarès* and Lluis F. Marsal*

Department of Electronic, Electric and Automatic Engineering, Universitat Rovira I Virgili, 43007 Tarragona, Spain
E-mail: josep.pallares@urv.cat and lluis.marsal@urv.cat

Abstract

Impedance spectroscopy (IS) has been widely applied to study organic solar cells (OSCs) device performance in the past few decades. IS allows the characterization in a broad range of time scales to extract information about internal process occurred within OSCs. However, most of the characterization were performed under standard AM 1.5G illumination–known as outdoor performance. Recently, the potential application OSCs under indoor energy harvesting have attracted great interest. In this work, IS analysis was used to study the reason of enhanced power conversion efficiency (PCE) enhancement in indoor (LED 2700 K 250—2000 lux) performance of inverted OSCs based on bulk heterojunction PTB7-Th:$PC_{70}BM$ in the device structure of ITO/TiOx/PTB7-Th:$PC_{70}BM/V_2O_5$/Ag compare to the outdoor performance counterparts.

1. Introduction

Organic solar cells (OSCs) have been the topic of a huge amount of research in the last few decades due to their low-cost, solution processed, less toxic, and light-weight.[1]–[3] Some strategies have been employed to boost their power conversion efficiency (PCE) of up to over 18% in a single junction bulk heterojunction OSCs under AM 1.5G illumination at 100 mW/cm^2 intensity.[4] In fact, these conditions were seldom to perform in outdoor application and especially not for indoor or low lighting applications.[5] Several researcher groups found that OSCs have a future prospective as indoor energy harvester for the Internet of Things application. [6], [7] A high PCE of up to 28% under LED lamp have been achieved.[8] However, a deep understanding of the fundamental mechanisms that take place under operation is still required to further optimize the performance of OSCs both under outdoor and indoor illumination.

IS method can measure the complex dielectric properties of material by a perturbed a small frequency-modulated (AC) signal which is applied in addition to a stationary (DC) voltage in term of frequency spectrum. The extracted frequency-dependent impedance can be interpreted in terms of the equivalent circuits model with resistive/capacitive (RC) elements to describe the internal processes of OSCs occurring at different time scales.[9]

In this work, IS analysis was used to study the reason of enhanced power conversion efficiency (PCE) enhancement in indoor (LED 2700 K 250—2000 lux) performance of inverted OSCs based on bulk heterojunction PTB7-Th:$PC_{70}BM$ in the device structure of ITO/TiOx/PTB7-Th:$PC_{70}BM/V_2O_5$/Ag compare to the outdoor performance counterparts.

2. Results and Discussion

An inverted device architecture of ITO/TiOx/PTB7-Th:$PC_{70}BM/V_2O_5$/Ag was fabricated to study the device performance under AM 1.5G illumination (outdoor 1 sun, 100 mW/cm^2) and LED 2700 K (indoor, 1000 lux) illumination. Fig. 1 shows the current density–voltage (*J-V*) characteristics with different illumination. The device performances such as short-current circuit (J_{SC}), open-circuit voltage (V_{OC}), fill factor (FF) and power conversion efficiency (PCE) are summarized in Table 1. The devices illuminated under AM 1.5G illumination showed a PCE of 9.71% with a J_{sc} of 17.06 mA/cm^2, a V_{oc} of 0.79 V and an FF of 72.03%. When illuminated under LED warm-light type 2700 K lamp, PCE was

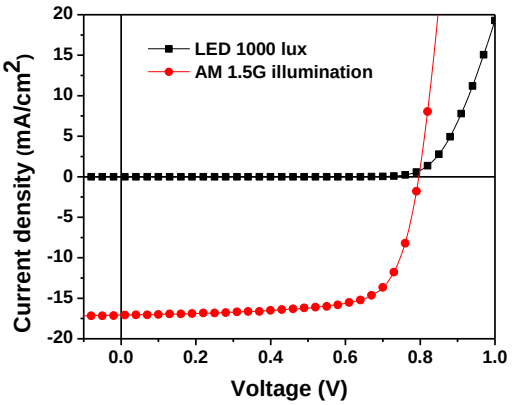

Fig.1. Current density versus voltage (*J-V*) characteristics of PTB7-Th:$PC_{70}BM$-based OSCs using TiOx as ETL under outdoor (AM 1.5G) and indoor illumination.

Illumination	V_{OC} [V]	J_{SC} [mA/cm^2]	FF [%]	PCE [%]
AM 1.5G	0.79	17.06	72.03	9.71
LED 1000 lux	0.66	0.12	71.21	13.83

Table 1. Device performance parameters of PTB7-Th:$PC_{70}BM$-based OSCs using TiOx as ETL under outdoor (AM 1.5G) and indoor illumination.

improved to 13.83% with a J_{sc} of 0.12 mA/cm^2, a V_{oc} of 0.66 V and an FF of 71.21%.

Even though *J-V* curves show a distinct behavior in their shapes, the information about the effect of different illumination on each layer is not yet well developed. Fig. 2 shows the Cole-cole plots of impedance spectra taken at 0V (short-circuit) bias voltage. All plots show typical arc behavior, more prominent under 1 sun, while under LED the arc is not a perfect semicircle due to the noise appeared under low light intensity. This semicircle shape suggests the presence of different resistive/capacitive (RC) component in the spectra.[9] As shown in inset Fig. 2, 3RC equivalent circuit model can provide information which layer are most affected by different illumination condition. By calculating the capacitance in each RC equivalent circuit, it allows to identify the resistance in each layer. Based on the RC equivalent fitting and calculation, different illumination does not affect the capacitance but the resistance does. The bulk layer of the devices under LED illumination has 3~4 orders magnitude higher than those of under 1 sun condition, indicating the bulk active layer has a significant role in determining the device performance under different lighting conditions.

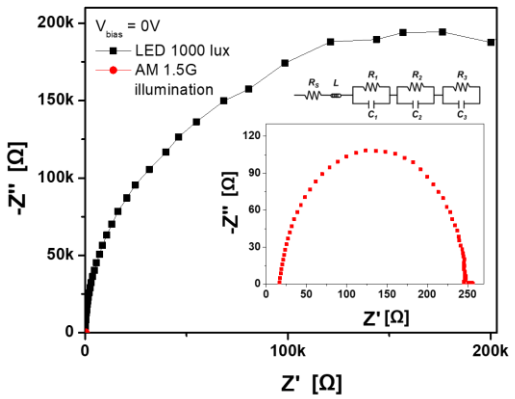

Fig.2. Cole-cole plots of PTB7-Th:$PC_{70}BM$-based OSCs using TiOx as ETL under outdoor (AM 1.5G) and indoor illumination

3. Conclusion

In conclusion, the different behaviour of inverted OSCs based on bulk heterojunction PTB7-Th:$PC_{70}BM$-based iOSCs performance under outdoor (AM 1.5G condiiton) and indoor (LED 2700 K) illumination can be observed by impedance spectroscopy analysis. IS is a powerful technique to identify which layer may play an important role to determine the device performance under different lighting conditions: bulk active layer.

References

[1] J. Zhang, H. S. Tan, X. Guo, A. Facchetti, and H. Yan, "Material insights and challenges for non-fullerene organic solar cells based on small molecular acceptors," *Nat. Energy*, vol. 3, no. 9, pp. 720–731, 2018.

[2] A. A. A. Torimtubun, J. G. Sanchez, J. Pallares, and L. F. Marsal, "Study of the Degradation of PTB7-Th:PC 70 BM-based Solar Cells using TiO x as Electron Transport Layers under Ambient Environment," in *2020 IEEE Latin America Electron Devices Conference (LAEDC)*, 2020, pp. 1–4.

[3] J. G. Sánchez *et al.*, "Impact of inkjet printed ZnO electron transport layer on the characteristics of polymer solar cells," *RSC Adv.*, vol. 8, no. 24, pp. 13094–13102, 2018.

[4] Q. Liu *et al.*, "18 % Efficiency organic solar cells," *Sci. Bull.*, vol. 65, no. 4, pp. 272–275, 2020.

[5] M. Kasemann, L. M. Reindl, and K. Rühle, "Photovoltaic Energy Harvesting under Low Lighting Conditions," *Proc. Sens. 2013*, pp. 483–485, 2013.

[6] A. A. A. . Torimtubun, J. G. . Sánchez, J. Pallarés, and L. F. Marsal, "Cathode Interface Engineering Approach for a Comprehensive Study of the Indoor Performance Enhancement in Organic Photovoltaic," *Sustain. Energy Fuels*, pp. 1–12, 2020.

[7] I. Mathews, S. N. Kantareddy, T. Buonassisi, and I. M. Peters, "Technology and Market Perspective for Indoor Photovoltaic Cells," *Joule*, vol. 3, no. 6. 2019.

[8] H. K. H. Lee *et al.*, "Organic photovoltaic cells-promising indoor light harvesters for self-sustainable electronics," *J. Mater. Chem. A*, vol. 6, no. 14, pp. 5618–5626, 2018.

[9] E. Osorio *et al.*, "Degradation Analysis of Encapsulated and Nonencapsulated TiO2/PTB7:PC70BM/V2O5 Solar Cells under Ambient Conditions via Impedance Spectroscopy," *ACS Omega*, vol. 2, no. 7, pp. 3091–3097, 2017.

Optical characterization of Nanoporous anodic alumina gradient index filters modified with Rhodamine 6G dye

Pankaj Kapruwan, Josep Ferré-Borrull*, Lluís F. Marsal*

Engineering. Electrònica, Elèctrica i Automàtica, Universitat Rovira i Virgilli, 43007, Tarragona, Spain

*Email: josep.ferre@urv.cat, lluis.marsal@urv.cat

Abstract

Porous materials have been an intense topic of research in the past several years and to the date serves as one of the best templates to be used in drug delivery applications. Amongst, several nanoporous structures, enormous developments have been reported of widely known Nanoporous anodic alumina gradient index filters (NAA-GIFs). This study aims to fabricate different nanoporous anodic alumina gradient-index filters (NAA-GIFs) with finely tuned engineering of multiple photonic stopbands (PSB) positioned at specific wavelengths. These NAA-GIFs are developed by modified sinusoidal anodization of aluminium in oxalic acid. Different types of NAA-GIFs having two desired peaks ranging in the visible spectral regions are produced. Subsequently, these NAA-GIFs are infiltrated by dropping Rhodamine dye on the surface. Before and after drying, reflectance measurements were recorded and their ratio between them has been analyzed in order to obtain a comprehensive idea regarding the filling inside the nanoporous channel. Simulation analysis has also been carried out to confirm the molecular behavior.

1. Introduction

Amongst the porous structures, nanoporous anodic alumina (NAA) is a material that offers ease of fabrication, mechanical robustness, widely tuneability of surface chemistry and stable optical properties [1-3]. Recent developments in NAA pore engineering have made it possible to develop numerous optically active templates (e.g. distributed Braggs reflectors, gradient-index filters, etc.) Propagation of light in these photonic structures can be achieved by the precise engineering of structural components of photonic structures. In order to develop drug delivery systems based on NAA, it is necessary to develop reliable methods to measure the loading and release profile of drug within the nanopores. To achieve this, NAA-GIFs are promising structures that can be designed to show photonic stop bands at desired spectral regions.

In this work, we use NAA-GIFs as a platform to reveal information about the molecular loading inside the nanoporous channels. For this purpose, as a model molecule, we have chosen the Rhodamine 6G dye and designed the photonic stop bands of the NAA-GIFs according to the absorption band of this molecule.

2. Experimental section

Materials: High purity aluminium discs (Al) (thickness, 0.5 mm and purity 99.99 %) were purchased from Good fellow Cambridge ltd. (U.K.), acetone ($(CH_3)_2CO$), ethanol (C_2H_5OH), perchloric acid ($HClO_4$), oxalic acid ($H_2C_2O_4$), Hydrochloric acid (HCl), copper chloride ($CuCl_2$) were provided by Sigma Aldrich. Double deionized water (DI) (18.6 MΩ) was used for all the solutions unless otherwise specified.

Fabrication: NAA-GIFs were prepared by following the procedure described elsewhere [4]. In brief, the samples fabricated in this study were obtained by anodization of aluminium in 0.3 M oxalic acid electrolyte at 5 °C. The current during anodization was periodically varied using the following parameters: J_0 = 2.6 $mAcm^{-2}$, J_1= 1.3 $mAcm^{-2}$, T_1= 165 s, T_2 = 250 s and N = 200 periods. After fabrication, the remaining aluminium was etched from the back side using a solution of copper chloride ($CuCl_2$) and hydrochloric acid (HCl). Next, the loading of the pores was performed by successive repetitive cycles of drop casting 10 µl of Rhodamine solution (1 mg/ml) onto the surface of NAA-GIFs and drying at room temperature. Before and after each cycle, the reflectance of the samples was measured in three replicates and at different positions.

3. Results and Discussion

Figure 1 shows a top view and a cross-section ESEM view (a and b, respectively) of one of the prepared NAA-GIFs.

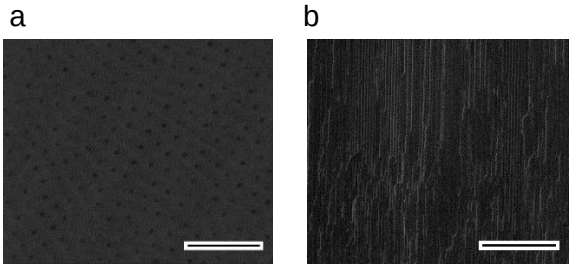

Figure 1: a & b) ESEM top and cross section of the NAA-GIFs respectively. Scale bar 1µm

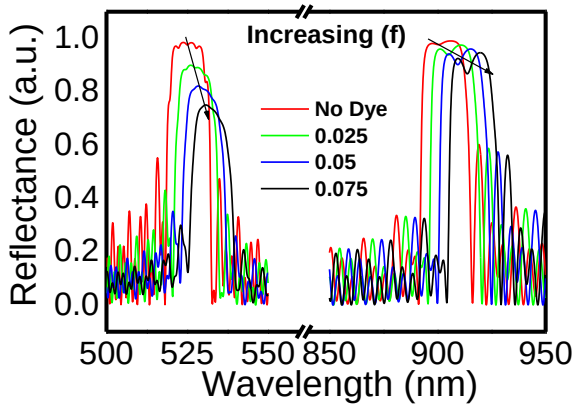

Figure 2 depicts simulation measurement of different dye amount inside NAA-GIFs.

Simulations show (Figure 2) that different amounts of dye inside the pores can be estimated by measuring the relative height of the maximum reflectance corresponding to the two stop bands which changes at a different rate.

Figure 3a represents UV-Vis reflectance spectra of one NAA-GIF sample after each drop/dry cycle. A clear decreasing trend with the number of drops is observed for both the peaks. Figure 3b plots the height (defined as maximum reflectance) of the first and second peak as a function of the number of drops where the decreasing trend can be explained by the fact that the molecule is accumulating inside the pores, and consequently influencing the maximum reflectance. Figure 3c shows a plot of the ratio between the Peak 1 height to Peak 2 height, as a function of the number of drops. This ratio is a good metric to analyze the relative decrease of the peak heights.

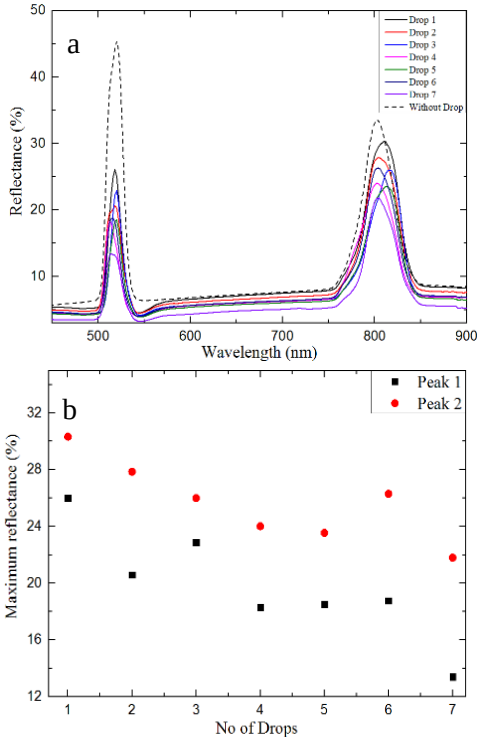

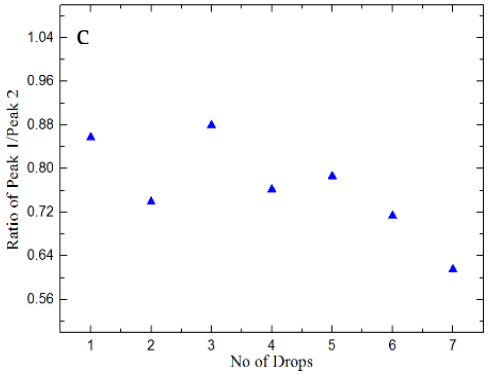

Figure 3.a) shows reflectance spectrum after each drop of dye; b) Plot of maximum reflectance vs number of drops; c) Ratio of Peak 1/Peak 2.

4. Conclusions

Here in we demonstrate the periodically engineered rugate structures and their subsequent filling with rhodamine dye using drop/dye cycle. This filling has been studied using reflectance measurements to extract information about the filling process and the data has been further analyzed to evaluate the molecular load inside the nanopores by comparing the height changes of the peak. A ratio between both the peaks has been established and considered one of the important parameter to be investigated in further experiments to gather release dynamics of the dye. In addition, dye/drop method has also been shown as an efficient method to fill the pores.

5. Acknowledgement

This work was partially supported by the Spanish Ministerio de Ciencia, Innovación y Universidades (MICINN/FEDER) RTI2018-094040-B-I00, by the Agency for Management of University and Research Grants (AGAUR) ref. 2017-SGR- 1527 and by the Catalan Institution for Research and Advanced Studies (ICREA) under the ICREA Academia Award.

6. References

1) Macias G, Ferré-Borrull J, Pallarès J, Marsal LF. Nanoscale Res Lett. 2014;9(1):1-6.
2) Porta-i-Batalla M, Xifré-Pérez E, Eckstein C, Ferré-Borrull J, Marsal LF. Nanomaterials. 2017;7(8):227.
3) Rahman MM, Marsal LF, Pallarès J, Ferré-Borrull J. ACS Appl Mater Interfaces. 2013;5(24):13375
4) Acosta LK, Bertó-Roselló F, Xifre-Perez E, Santos A, Ferré-Borrull J, Marsal LF. ACS Appl Mater Interfaces. 2019;11(3):3360

New peak annotation tool for the rMSIproc MSI processing package highlights and ranks monoisotopic and adduct-related ions.

Lluc Sementé[1], Pere Ràfols[1,2,3], Mari García-Altares[1,3], Gerard Baquer[1], Xavier Correig[1,2,3]

[1] Department of Electronic Engineering, Rovira i Virgili University, Tarragona, Spain;
[2] Institut d'Investigació Sanitària Pere Virgili, Tarragona, Spain;
[3] Spanish Biomedical Research Centre in Diabetes and Associated Metabolic Disorders (CIBERDEM), Madrid, Spain;

1.Introduction

Mass spectrometry imaging (MSI) localizes the chemical compounds of a biological tissue and produces an extensive collections of spectral data. The spectra are stored in large datasets that contain all the signals coming from each chemical compound. As chemical compounds produce more than one signal (isotopes, adducts, fragments, etc.) both informative and redundant information is stored [1]. This enlarges the datasets, complicates compound identification and harms multivariate statistical tests. A solution can be approached using peak annotation algorithms. Currently, only two tools are abaliable for this purpose: MassPix [2] and Metaspace [3]. Here, we present a new open-source peak annotation tool for the rMSIproc packager[4]. The engine's algorithm identifies carbon monoisotopic ions, searches for adduct ions and provides quality information for each annotated signal. The resulting information speeds up and simplifies the identification process.

2.Method

The algorithm input is an rMSIproc peak matrix where, rows represent pixels and columns represent m/z species. For each column, the algorithm generates isotope candidates and evaluates them using three metrics: image morphology, isotopic profile matching and peaks centroids mass deviations. This produces a list of monoisotopic candidates with a likelihood score. The candidates surpassing the user's threshold are considered robust isotopic patterns and directed to the adduct pairer, which searches mass differences coinciding with a user-provided adduct list. The annotation engine produces three levels of annotations. Level A contains neutral masses produced by pairs of monoisotopic ions, Level B contains neutral masses produced by one monoisotopic ion and one non-annotated ion and level C contains all the monoisotopic ions detected by the algorithm. The algorithm was tested using an in-house synthetic dataset containing multiple signals of various molecules and two experimental datasets with previously identified compounds. The first experimental dataset consist of ovarian follicles of cows analyzed using a TOF mass analyzer. The second experimental dataset consist of an alga with a viral infection analyzed using a FT-ICR mass analyzer. The datasets were imported to imzML, processed using rMSIproc's workflow and supplied to the annotation engine.

3.Results

The program's execution took a few seconds to produce high quality annotations matching some of the MS/MS identifications. For the TOF dataset, 23 compounds were annotated from the list of 43 identified by the authors. For the FT-ICR dataset, 28 compounds were annotated from the list of 37 identified by the authors. Moreover, additional annotations were obtained, this allowed to produce new tentative molecular assignments, 13 for the TOF dataset and 28 for the FT-ICR dataset, increasing the biological information retrieved from the tissue.

4.Conclusions

The presented peak annotation tool, designed with optimized resource management, allows fast and confident peak annotations for MSI datasets. This enables researches to obtain MSI molecular annotations easily and reliably, which helps in the later identification procedure.
With the addition of this new tool, rMSIproc is capable of completely processing any MSI dataset from raw data to a peak matrix with annotations.

5.References

[1] L. A. McDonnell, A. van Remoortere, N. de Velde, R. J. M. van Zeijl, and A. M. Deeldera, "Imaging mass spectrometry data reduction: Automated feature identification and extraction," *J. Am. Soc. Mass Spectrom.*, vol. 21, no. 12, pp. 1969–1978, 2010.

[2] N. J. Bond, A. Koulman, J. L. Griffin, and Z. Hall, "massPix: an R package for annotation and interpretation of mass spectrometry imaging data for lipidomics," *Metabolomics*, 2017.

[3] A. Palmer *et al.*, "FDR-controlled metabolite annotation for high-resolution imaging mass spectrometry," *Nat. Methods*, vol. 14, no. 1, pp. 57–60, Jan. 2017.

[4] P. Ràfols *et al.*, "rMSIproc: an R package for mass spectrometry imaging data processing," *Bioinformatics*, vol. 36, no. 11, pp. 3618–3619, 2020

Optimizing ZnO Thin Film by Spray Pyrolysis Deposition Technique for High Performance Inverted Polymer Solar Cells

Enas Moustafa*, Lluis F. Marsal, and Josep Pallarès

Department of Electric, Electronic, Engineering and Automatic, Universitat Rovira i Virgili, 43007, Tarragona, Spain.

E-mail: enas.moustafa@urv.cat*, lluis.marsal@urv.cat, josep.pallares@urv.cat,

Abstract

In this research work, noteworthy progress has been achieved to fabricate efficient inverted polymer solar cells (iPSCs) using simple and low cost spray pyrolysis (SP) technique to deposit a thin film of ZnO as electron transporting layer (ETL). The concentrations of the ZnO precursor solution and spraying procedures by the SP technique have been studied to obtain the optimal conditions that allow achieving high iPSCs performance. Moreover, standard iPSCs fabricated by spin coating (SC) technique has been used as a reference cells. It has been observed that the performance of the iPSCs fabricated by ZnO- SP were quite similar to the reference samples fabricated by the ZnO-SC technique. Hence, this promising spray pyrolysis technique might be a breakthrough forward step for commercializing the inverted polymer solar cell based on mass production.

1. Introduction

Polymer solar cells have been extensively investigated as a promising third generation solar cells alternative to the inorganic materials due to their flexibility, low fabrication cost, light weight and being capable of engaging with other electronic applications. [1]. Zinc oxide (ZnO) is one of the typical oxides utilize as electron transport layers (ETL) in the iPSCs [2]. The deposition method for the ETL layers is an important factor which should be mentioned as it influences the interfaces between the layers and the film surface morphology. Spray pyrolysis technique (SP) is widely used for thin film deposition which matches the industrial mass production not only lab-scale. Moreover, it is a low cost, facile technique that does not require any vacuum or complicated conditions [3]. In this research work, SP technique has been used to prepare a thin film of ZnO-ETL to be used in the fabricate iPSCs with the structure of ITO/ZnO/ PTB7-Th: $PC_{70}BM$/ V_2O_5/Ag. In addition, iPSCs fabricated by SC technique to deposit the ZnO film (ZnO-SC) to be the controlling reference cells. The great gain in this work is that iPSCs fabricated by the SP have achieved high performance quite similar to the reference cells prepared by lab-scale SC technique.

2. Experimental Methods

The transparent conducting oxide used was indium tin oxide (ITO)-patterned glass substrate with a resistivity of 10 Ω sq^{-1} from PsiOTec Ltd. For synthesis the ZnO-ETL precursor solution, zinc acetate dihydrate 99.999% (A-Aldrich), 2-methoxyethanol 99.9% (Sigma Aldrich) and ethanolamine 99.5% (A-Aldrich) were purchased. The donor polymer PTB7-Th and the fullerene acceptor $PC_{70}BM$ were bought from One-Material Inc and Solenne BV. V_2O_5 used as HTL which Sigma Aldrich with 99.999% purity and the Ag from Testbourne Ltd.

2.1 Device Fabrication

The fabricated devices have the structure of ITO/ZnO /PTB7-Th: $PC_{70}BM$/V_2O_5/Ag. The ITOs have been cleaned by subsequent ultrasonicated detergent in water, acetone, methanol; and isopropanol then treated by UV-Ozone. Followed by ZnO solution deposition which has been synthesized by adding 0.68M of zinc acetate dihydrate and 0.46M of ethanolamine to 2-methoxyethanol, then the mixture was left for 1 hr stirring at 70ºC [4]. The synthesized solution was diluted by methanol 1:1 v/v ratio to prepare a stock solution. For the spin coating technique, the ZnO stock solution was spun at 3000 rpm for 30 secs, then kept for 1 hr to be annealed at 200 ºC [5]. For depositing the ZnO solution using spray pyrolysis technique, two concentrations have been used [6]. Concentration A which is the low concentration prepared by diluting the synthesized stock solution with ethanol by 0.5:9.5 v/v. The other high concentration B with the ratio of 1:6 v/v. Concentrations A and B were deposited over the pre-heated ITO at 350ºC and the sprayed films left to anneal for 1 hr. The active polymer blend was prepared by dissolving 25 mg/ml of PTB_7-Th:$PC_{70}BM$ 1:1.5 w/w in chlorobenzene and DIO with the ratio of 97: 3 % v/v. Then the blend filtered and spun over the ZnO film at 750 rpm for 30 secs. Finally, V_2O_5 and Ag films were deposited by thermal evaporation under high vacuum conditions.

2.2 Device Characterization and Measurements

Current density-voltage (J-V) characteristics of the fabricated iPSCs have been characterized at room temperature under illumination of 1.5 AM and with keithley 2400 source-measure unit. The illumination condition has been produced by the solar simulator (Abet Technology model 11000 class type A, Xenon arc).

3 Results and Discussion

In this research work, two different concentrations with different numbers of running cycles have been investigated to deposit the ZnO film by the SP technique to optimize the conditions for the iPSCs as well comparing with the reference cells fabricated by the SC-lab technique. The low concentration A has been deposited with high number of running cycles 20R, while the high concentration B has been deposited with low number of running cycles 7R.

Fig. 1 illustrates the illuminated current density-voltage (J-V) characteristics of the iPSCs fabricated by SP and SC techniques. In addition, Table I shows their performance parameters: open-circuit voltage (V_{OC}), short circuit current density (J_{SC}), fill factor (FF), power conversion efficiency (PCE), the series (R_S) and parallel (R_P) resistance values. From the obtained results it can be noticed that, all the fabricated cells have almost the same V_{OC}. It is worth mentioning that the generated J_{SC} for the iPSCs fabricated by the ZnO sprayed using SP technique was higher than the ones deposited by SC technique. However ZnO-SP sprayed A and B iPSCs suffer from the higher leakage current which confirmed by higher R_S and lower R_P than the ZnO-SC reference as shown in Table.1. Although both A and B ZnO-SP iPSCs provided high performance which is quite similar to the reference one deposited by SC. But, the B-7R obtained higher R_P and J_{SC} which indicates that at higher concentration a dense surface might be start to perform which decrease the leakage and increase the generated current by enhancing the current path to flow which in turn improves the cell performance.

Samples	V_{OC} (V)	J_{SC} mA/cm^2	FF %	PCE %	R_S Ω.cm^2	R_P Ω.cm^2
ZnO-SC	0.79	17.85	73.0	10.29	1.05	1180
SP-A20R	0.80	18.29	67.0	9.83	2.46	608
SP-B7R	0.79	18.78	67.3	9.96	2.49	616

Table1. Solar Cells Performance parameters for the iPSCs Fabricated by SC and SP Techniques.

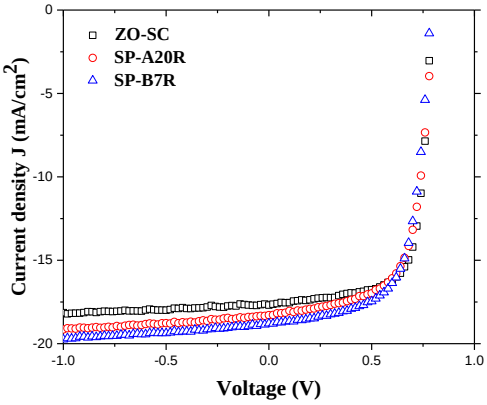

Fig.1. J-V characteristic curves for ZnO thin film by SC and SP under illumination.

4. Conclusions

It can be summarized that iPSCs fabricated using ZnO-ETL obtained by the spray pyrolysis technique have properly similar performance compared to the cells fabricated by the usual lab-scale spin coating technique, achieving devices efficiency close to 10 %. Moreover, the SP-B7R iPSCs have better performance than the SP-A20R which might be attributed to the higher concentration that performed more dense film. Consequently, using the spray pyrolysis technique is promising, simple and cost effective tool. In addition, the ability to control the deposition parameters is facile and reproducible. The illustrated work is an initial result observed for the spray pyrolysis technique to deposit a thin film of ZnO-ETL for iPSCs and the optimization for more parameters is proceeding.

References

[1] S. K. Hau, H. L. Yip, A. K. Jen, "A Review on the Development of the Inverted Polymer Solar Cell Architecture," Polymer Reviews J, vol. 50, no. 4, pp. 474–510, Nov. 2010.

[2] M. Ramírez-Como, V.S. Balderrama, A. Sacramentoa, L.F. Marsal, G. Lastra, M. Estrada, "Fabrication and characterization of inverted organic PTB7:PC_{70}BM solar cells using Hf-In-ZnO as electron transport layer," Solar Energy, vol. 181, no. 38, pp. 386-395, Mar. 2019.

[3] A. Tecaru, A. I. Danciu, V. Muşat, E. Fortunatoa, E. Elangovan, "Zinc oxide thin films prepared by spray pyrolysis," Optoelectronics and Advanced Materials J, vol. 12, no. 9, pp. 1889 – 1893, Sep. 2010.

[4] J. G. Sánchez, V. S. Balderrama, S. I. Garduño, E. Osorio, A. Viterisi, M. Estrada, J. F-Borrull, J. Pallarès and L. F. Marsal, "Impact of inkjet printed ZnO electron transport layer on the characteristics of polymer solar cells," RSC advanced, vol. 8, no. 24, pp. 13094–13102, Mar. 2018.

[5] G. Lastra, V. S. Balderrama, L. Reséndiz, J. Pallarès, S. I. Garduño, V. Cabrera, L. F. Marsal, M. Estrada, "High-Performance Inverted Polymer Solar Cells: Study and Analysis of Different Cathode Buffer Layers," *IEEE Journal of Photovoltaics*, vol. 8, no. 2, pp. 505-511, pp. 150, Mar. 2018.

[6] Enas Moustafa, J. G. Sánchez, L. F. Marsal and J. Pallarès, "Deposition Technique for Inverted Polymer Solar Cells Using ZnO-ETL", IEEE 2020 LAEDC, Feb. 2020.

NO_2 Gas sensing based on Pulsed UV light and FFT analysis using MOX sensors

Ernesto González Fernández

Departament d'Enginyeria Electrònica, Elèctrica i Automàtica
ernesto.gonzalez@urv.cat

Abstract

In this work, we present the first known development of calibration models, using pulsed UV light modulation for WO3 based gas sensing. Partial Least Squares Regression (PLSR) and Principal Component Regression (PCR) methods have been developed using components from the FFT analysis of the DC resistance signal of the sensor. The use of pulsed UV light combined with low-temperature activation allowed a significant reduction in power consumption as compared to the high operating temperature traditionally used with Metal Oxide non-MEMs-based sensors.

1. Introduction

For many years, MOX sensors have been typically used by applying operating temperatures in the range 100-500 ºC to improve their response and sensitivity, which implies a considerable power consumption to heat the sensors [1]. However, a few years ago, the UV-irradiation of MOX sensors has been studied as an alternative to the more traditional thermally activated gas sensing [2]. UV light provokes the generation of electron/hole pairs, induced by the photoconductivity effect, which increases the density of charge carriers through the semiconducting layer, improving the absorption/desorption mechanism [3]. On the other hand, several researchers have used mathematical data analysis and statistical methods to quantify the concentration of a target gas and determine the Limit of Detection (LOD) of MOX sensors [4]. The use of Principal Component Analysis (PCA), and the development of calibration models using Principal Component Regression (PCR) and Partial Least Square Regression (PLSR) have permitted to determine the target gas concentration in gas sensing applications (e.g., CO, NO2, volatile compounds, among others) [5]. While most of these studies have implemented the data analysis methods using the DC signal of the sensors working under temperature modulation [4], some researchers have reported the use of components from the Fast Fourier Transform (FFT) analysis of the resistance transients as input data for these analysis methods. This methodology has become an excellent tool for determining gas concentration and discriminating different gases [6].

This work presents the development of calibration models of a tungsten trioxide (WO3) based pulsed UV light modulated gas sensor, based on the above-mentioned research background. Combined low temperature and pulsed UV light configuration are used for measuring NO2 at ppb level. The FFT components from the analysis of the resistance signal of the sensors are used as input of the PCR and PLSR methods.

2. Description of the method

In order to generate a model which allows us to identify the concentration of studied gas, mathematical and computational tools were used, such as, FFT, PCR, and PLSR. All data analysis was carried out by using MATLAB R2017b. Fig. 1 shows the flow diagram of the data analysis process. We propose to apply a frequency domain analysis to the sensor signal, which, due to the UV modulation, shows a ripple superimposed to the electrical resistance change due to gas exposure. After taking vectors from the time domain signal with 2, 4 and 9 UV light periods from each gas concentration, we computed an FFT of each one in order to perform a frequency domain analysis. FFT vectors were manipulated in order to remove components that did not provide relevant information. For this purpose, we analyzed what other components, apart from the direct component (0 Hz), appeared in spectra. We found that a component corresponding to UV light switching period (for 60 s period the corresponding frequency is 0.01667 Hz) and its even order harmonics appeared in the FFT spectrum. Therefore, we generated a new vector, which contained just values corresponding to the frequencies of interest (ON/OFF frequency and a set of its even order harmonics) in order to reduce the amount of data used in the modeling process and, in this way, avoid using low-intensity frequency components that may be prone to be affected by noise. Finally, we used just the UV light switching frequency and its 2 first even order harmonics as using a higher amount of FFT components did not improve the prediction error or the standard deviation of the model. We constructed a

training matrix containing concatenated vectors for each concentration. In this matrix, rows are different concentrations and columns are frequency components of interest. This training matrix were used to develop the PLSR and PCR calibration models.

We used cross validation to estimate the accuracy of the different models to predict NO2 concentrations. Thus, we applied a leave-one-out strategy, leaving all the data about one of the studied concentrations out of the training set, and using it as validation set each time.

RMSE and R2 results obtained for PLSR and PCR models using UV light ON/OFF periods of 60 s and 30 s with NO_2 concentrations from 900 to 37.5 ppb are presented in Table 1. Figure 2 depicts calibration model and validation results for a training matrix constructed with FFT components from 9 UV light pulses from the time domain signal.

Model	Period [s]	Range [ppb]	RMSE [ppb]	R^2
PCR	60	200-900	52.7	0.9454
PLSR	60	200-900	55.6	0.9454
PCR	30	300-900	71.0	0.9035
PLSR	30	300-900	71.1	0.9033
PCR	30	37.5-150	10.5	0.94.91
PLSR	30	37.5-150	10.5	0.9491

Table 1. Models´ RMSE and R-squared values from 4 pulses analysis for validation process.

3. Conclusions

We have proposed the combined use of FFT analysis and linear regression methods to obtain calibration models that allow us to determine NO_2 concentrations using a WO3 based sensor. The combined pulsed UV light and low-temperature heating configuration used as activating mechanism represents a reduction in power consumption of about 90% as compared to the traditional heating mechanism at 250 ºC. This approach also allows a reduction of the response time, since the concentration can be determined without requiring the sensor resistance to reach the steady state value. Moreover, R^2 values over 0.94 were obtained for concentrations under the exposure limits defined for nitrogen dioxide.

References

[1] D. Zappa, V. Galstyan, N. Kaur, H. M. M. Munasinghe Arachchige, O. Sisman, and E. Comini, "'Metal oxide -based heterostructures for gas sensors'- A review," Anal. Chim. Acta, vol. 1039, pp. 1–23, 2018.

[2] J. D. Prades et al., "Equivalence between thermal and room temperature UV light-modulated responses of gas sensors based on individual SnO2nanowires," Sensors Actuators, B Chem., vol. 140, no. 2, pp. 337–341, 2009.

[3] F. Taghipour, "UV-LED Photo-activated Chemical Gas Sensors: A Review AU - Espid, Ehsan," Crit. Rev. Solid State Mater. Sci., vol. 42, no. 5, pp. 416–432, Sep. 2017.

[4] J. Burgués and S. Marco, "Multivariate estimation of the limit of detection by orthogonal partial least squares in temperature-modulated MOX sensors," Anal. Chim. Acta, vol. 1019, pp. 49–64, 2018.

[5] J. Burgués and S. Marco, "Low power operation of temperature-modulated metal oxide semiconductor gas sensors," Sensors (Switzerland), vol. 18, no. 2, 2018.

[6] A. Ghosh, A. Maity, R. Banerjee, and S. B. Majumder, "Volatile organic compound sensing using copper oxide thin films: Addressing the cross-sensitivity issue," J. Alloys Compd., vol. 692, pp. 108–118, 2017.

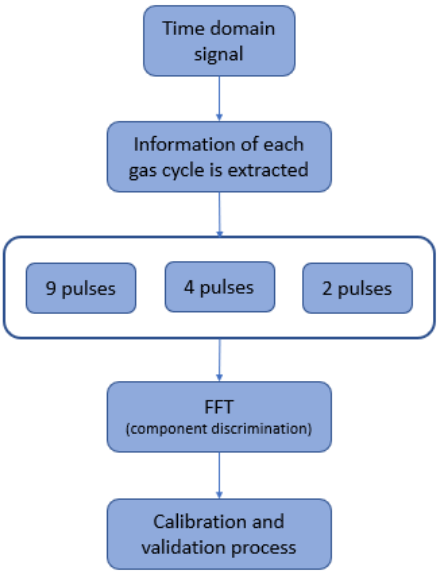

Fig.1. Flow diagram of the data analysis process.

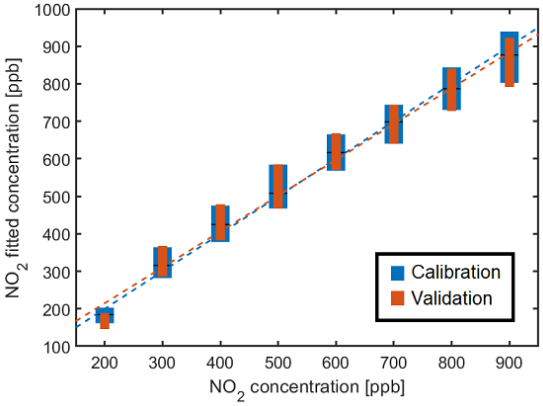

Figure 2. PLSR calibration model and cross-validation using 9 UV light pulses to perform the models. Blue boxes represent the dispersion of the calibration for each concentration and orange boxes represent the validation dispersion. Black lines are the calibration mean value for each concentration. The linear calibration fit and the linear validation fit are presented in blue and orange dashed lines, respectively.

Measurement of Time-Dependent Effects in DNTT-Based OTFTs

Christian Roemer, Ghader Darbandy, Jakob Leise, Jakob Pruefer, Alexander Kloes

***Abstract*—This document deals with bias-stress effects of organic field-effect transistors that are notable by changing device characteristics over time while a bias voltage is applied. The document shows some results of bias-stress measurements of dinaphtho[2, 3-b: 2', 3'-f]thieno[3, 2-b]thiophene-based organic thin-film transistors. Additionally, an explanation attempt of the measured effects is provided based on the theory that charge-carriers get trapped and immobilized within the organic semiconductor and cause a threshold voltage shift of those devices.**

I. Introduction

Organic electronics as a relatively new technology have become more and more popular over the last decades. This technology represents a low cost alternative to crystalline semiconductor electronics. However, the technology of organic semiconductors (OSCs) still has some drawbacks which must be considered in circuit-design. One major drawback of this technology which is investigated in this paper is the time dependency in the electrical characteristics of organic field-effect transistors. Several measurements showed that the drain-current of the tested dinaphtho[2, 3-b: 2', 3'-f]thieno[3, 2-b]thiophene (DNTT)-based organic thin-film transistors (OTFTs) changes over time during constant bias-voltage levels at the device terminals [1], [2]. The measured effects show that the device's characteristics are dependent on its bias-voltage history. The opinion on the cause of the time-dependent behavior varies in different publications and might also be a property of the used organic material itself. One common explanation for those effects that is found in references is that deep traps in the band-like structure of the OTFTs capture and release charge-carriers [3], [4].

II. Measurement Setup and Devices

The measurements of bias-stress effects (drain-current curve measured over time) of this work are done with the semiconductor device analyzer B1500A from Keysight Technologies Inc. The measured p-type inverted-staggered OTFTs (bottom-gate and top-contact) [5] are fabricated by the Max Planck Institute for Solid State Research in Stuttgart. The OSC material is DNTT with a channel thickness of $t_{ch} = 11\,\mathrm{nm}$ [5]. The gate is made of a $30\,\mathrm{nm}$ thick layer of aluminum and the source and drain contacts are made of $25\,\mathrm{nm}$ thick layer of gold [5]. The oxide/dielectric of the devices consists of an about $3.6\,\mathrm{nm}$ thick layer of aluminum oxide (AlO_x) and an about $1.7\,\mathrm{nm}$ thick self-assembled monolayer of n-tetradecylphosphonic acid [5]. Additionally, the device the measurements of which are shown in this document has a channel width of $W = 200\,\mu\mathrm{m}$ and a channel length of $L = 40\,\mu\mathrm{m}$.

This project is funded by a grant from TH Mittelhessen University of Applied Sciences, Giessen, Germany. We would like to thank the Max Planck Institute for Solid State Research, Stuttgart 70569, Germany for providing the fabricated devices

C.Roemer, G. Darbandy, J. Leise, J. Pruefer and A. Kloes are with NanoP, TH Mittelhessen University of Applied Sciences, 35390 Giessen, Germany (e-mail: chrisitan.roemer@ei.thm.de).

III. Measurement Results

Figure 1 (a) and 1 (b) show two different measurement setups that were performed on the tested device. Each measurement is done over a given amount of time and keeps one of the transistor's terminal voltages constant while the other one (that is not the source terminal) changes in the shown sequence. The first experiment shows the impact of gate-voltage changes on a measured device. This experiment is shown in figure 1 (a). The drain-voltage in this experiment was set at a constant level of $V_{ds} = -3\,\mathrm{V}$, while the gate voltage was sequenced. The rising (absolute) voltage-steps result in a current-degradation over time. After the first voltage-step to $V_{gs} = -1\,\mathrm{V}$ in the beginning, the effect is slightly noticeable. It gets bigger at the voltage-step to $V_{gs} = -2\,\mathrm{V}$ and even bigger at the voltage-step to $V_{gs} = -2.5\,\mathrm{V}$. In terms of trapping effects this measurement shows that a higher gate-voltage leads to more or a faster trapping of carriers. After the first voltage-step down, the current behavior turns around and becomes an increase of the absolute current. In terms of trapping effects, the gate-voltage steps down lead to a temporary de-trapping effect (emptying process of deep traps) of charge carriers.

The second test-scenario which is shown in figure 1 (b) consists of two phases of $V_{ds} = -3\,\mathrm{V}$ and a phase of $V_{ds} = 0\,\mathrm{V}$ in between. The gate-voltage does an initial step to $V_{gs} = -2.5\,\mathrm{V}$ in the beginning and remains on that level for the rest of the experiment. During the first on-phase, the current-degradation (or trapping effect) that is already shown before can be observed. After the phase without a drain-bias the current increases instead of decreasing (de-trapping behavior). This leads to the conclusion that an even higher rate of carrier trapping happens during the gate-only stress-phases.

IV. Conclusion

The measured bias-stress effects that are shown in this paper seem to be reversible. An attempt to explain this behaviour is due to a trapping-effect of positive charges in the bulk or in the

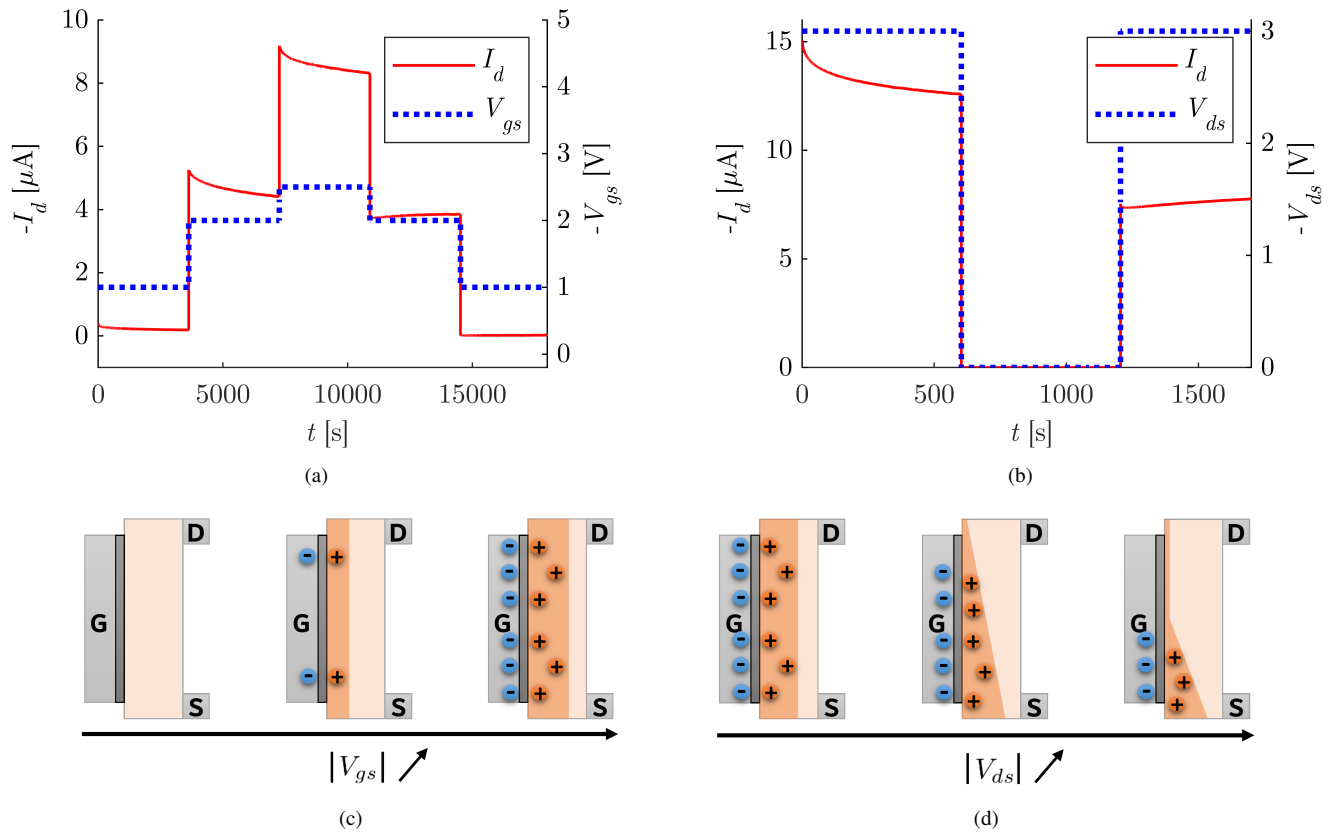

Figure 1. Measurements and visualized explanation attempt of the measured effects. (a) shows a test scenario where the drain-current I_d (red) is measured over time with a constant drain-voltage of $V_{ds} = -3\,\mathrm{V}$ and the shown gate-voltage V_{gs} sequence (blue). (b) shows a measurement with a constant gate-voltage of $-2.5\,\mathrm{V}$ and two drain-voltage on-phases. (c) shows the impact of a gate-bias voltage increase (more negative gate-bias) on charge trapping in the channel-region. The positive, orange charges located in the channel represent trapped charges. The negative, blue charges located in the gate are the needed charges that compensate the trapped charges. (d) shows the impact of a drain-bias voltage increase (more negative drain-bias) on charge de-trapping in the channel-region.

insulator region of the transistor. Those trapped charges lead to an electric field between them and charges with an opposite sign in the gate region. The electric field that is caused by the additional charges needs to be compensated by a higher gate voltage in order to accumulate more non-trapped charges in the device's channel region, which can contribute to the current flow. Therefore, it is estimated, that trapped charges increase the threshold voltage of the devices. The measurements show different impacts of V_{gs} and V_{ds} sequences on the drain current course of the device. A higher absolute gate voltage leads to a trapping behavior and a higher absolute drain voltage leads to a de-trapping behavior. An explanation attempt for this effect is shown in figure 1 (c) and (d). A more negative gate-voltage leads to a higher number of accumulated positive charges near to the semiconductor-insulator interface region. Suppose, there are positively charged traps in this region, the accumulation caused by the gate-bias would result in a higher trapping probability and therefore, in a higher number of trapped charges. Figure 1 (c) visualizes this effect.

An increase of the negative drain-voltage leads to a reduction of the accumulation channel size, which is shown in figure 1 (d). The drain-voltage induced accumulation-channel reduction could be a reason for a de-trapping effect. This would also explain the reversibility of those effects. This means that an absolute drain-voltage reduction leads to a trapping behavior and an absolute gate-voltage reduction leads to a de-trapping behavior again.

Additional measurements on bias-stress behaviour of such devices, which are beyond the scope of this document can be found in [2].

References

[1] G. Darbandy, C. Roemer, J. Leise, J. Pruefer, J. W. Borchert, H. Klauk, and A. Kloes, "Characterization of the charge-trap dynamics in organic thin-film transistors," in *2019 MIXDES - 26th International Conference "Mixed Design of Integrated Circuits and Systems"*. IEEE, jun 2019.

[2] C. Roemer, "Measurement-setups and evaluation of time-dependent effects in DNTT-based organic thin-film transistors," Master thesis, TH Mittelhessen University of Applied Sciences, Aug. 2019.

[3] F. Hain, M. Graef, B. Iñíguez, and A. Kloes, "Charge based, continuous compact model for the channel current in organic thin-film transistors for all regions of operation," *Solid-State Electronics*, vol. 133, pp. 17–24, jul 2017.

[4] R. Häusermann, "Fast and slow charge trapping and transport in organic semicondutors," Ph.D. dissertation, ETH Zürich, 2013.

[5] T. Zaki, S. Scheinert, I. Horselmann, R. Rodel, F. Letzkus, H. Richter, U. Zschieschang, H. Klauk, and J. N. Burghartz, "Accurate capacitance modeling and characterization of organic thin-film transistors," *IEEE Transactions on Electron Devices*, vol. 61, no. 1, pp. 98–104, jan 2014.

Numerical approach to input filter design for switching converters

Ramon Estalella, Angel Cid, Carlos Olalla

Universitat Rovira i Virgili

Abstract

Switching power converters often require input filters to reduce current and voltage ripple and to comply with conducted electromagnetic interference (EMI) regulations. The design of these filters is typically carried out by hand, using conservative constraints that allow to largely simplify the problem. This paper presents a numeric approach that can overcome these conservative constraints and may provide an optimal solution that is found automatically.

1. Introduction

When designing an input filter for a switching converter, the main goal is to comply with EMI limitations and limit the performance degradation that such filter could add to the overall system.

Since input filters are typically designed on top of existing converters, designers must consider the possible dynamic interactions that may arise, which may even lead to instability. Usually a second or third order filter is added to a converter, so that analysing the dynamics of the entire system can be challenging. For that reason conventional design approaches typically rely on simplifications of the stability criteria to assist on the process.

The basis for what can be considered conventional design is given by [1]. Our goal is to create a numerical method that matches or improves the conventional design method in performance of the overall system, while making the design of said filter easier and quicker. Another goal would be able to scale up the numerical method to systems of higher complexity.

2. Conventional design

The conventional way to tackle the problem consists of finding how a transfer function (TF) of interest, for example the control-to-output TF ($G_{vd}(s)$) changes when we add the filter. The objective is to try and minimize said change. After a series of considerations it is found that if the following inequalities are satisfied:

$$\|Z_N\| \gg \|Z_0\| \quad \|Z_D\| \gg \|Z_0\| \tag{1}$$

the filter does not substantially alter the control-to-output TF. We have impedance terms from the filter ($Z_0(s)$) and the converter ($Z_D(s)$ and $Z_N(s)$). This is a sufficient condition for stability (yet not necessary). If we wanted to be more strict with stability we should analyse the new TF for the exact conditions for stability.

Working with a simple case: we'll model the converter as an ideal CPL, this means that the dynamics that Z_D and Z_N could have, are gone. We have a single Z_{in} for the CPL which is defined as $Z_{in} = \frac{{V_{CPL}}^2}{P_{CPL}}$. The filter used is an RLC filter, with R in series with the inductance. Generally a series resistance in the path of the power transfer is not desired, but it is an interesting case since the intrinsic resistance of the inductance could be enough to stabilize the filter and also due to the low complexity of the LC filter.

Input voltage and power are uncertain parameters. The design criteria will be to obtain a certain attenuation at the switching frequency. The capacitor value is given. This means we have to obtain an inductance value to comply with the attenuation and the resistance value in order to stabilize the system and also undesired oscillations.

The design parameters for the filter are: $P = 1$ to $60\ W$, $V = 8$ to $12\ V$, $C = 1000\ \mu F$, $f_c = 100\ kH$ and attenuation at f_c to be at least $-60\ dB$.

In Figure 1, we see the magnitudes of the worst case input impedance for the CPL (Z_{in}), and that of the output impedance of the designed filter. In order to comply with inequalities (1), the magnitude of the filter must be well below (Z_{in}). In this case, we have selected a filter in which the magnitude of the filter is at least 20 dB below (Z_{in}). The designed values for the inductance and resistance are: $L_f = 2.6\ \mu H$ and $R_L = 30\ m\Omega$. Which gives us the desired attenuation at f_c and a damping ratio of $\zeta = 0.3$ and an efficiency of $97\ \%$.

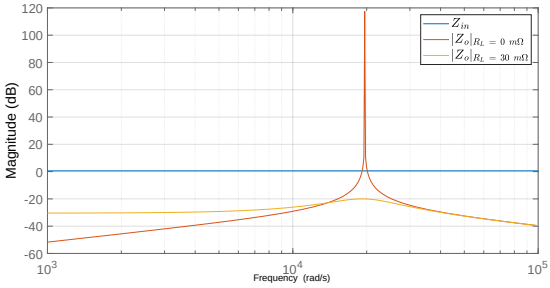

Figure 1: Magnitude Bode plot of the impedances for the conventional design process

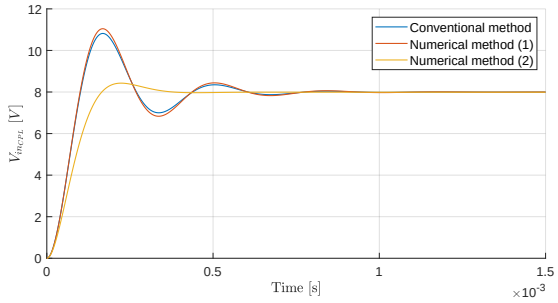

Figure 2: Step response of $V_{in_{CPL}}$

3. Numerical method

First we'll rewrite the problem in order to have a state feedback problem. The RLC filter with a CPL, has a linearised state space representation $\dot{x} = A_f x$ where:

$$A_f = \begin{pmatrix} -\frac{R_L}{L} & \frac{-1}{L} \\ \frac{1}{C} & \frac{P}{CV^2} \end{pmatrix}; \quad x = \begin{pmatrix} i_L \\ v_C \end{pmatrix} \tag{2}$$

We can then rewrite the system with a virtual state feedback representation: $\dot{x} = Ax + Bu = (A + BK)x$ where:

$$K = [K_1\ K_2] \tag{3}$$

$$A = \begin{pmatrix} 0 & 0 \\ \frac{1}{C} & \frac{P}{CV^2} \end{pmatrix}; \qquad B = \begin{pmatrix} \frac{-1}{C} \\ 0 \end{pmatrix} \tag{4}$$

$$R_L = \frac{K_1}{K_2}; \qquad L = \frac{-1}{B_1 K_2} \tag{5}$$

Now we have rewritten the system on a standard state feedback form, and we have a way to get our L and R_L values from the virtual state feedback vector K. The design of K is based on the constraint that the resulting system must be stable, and that the poles of the filter must be placed in a region that satisfies the required attenuation level and some dynamic specifications [2]. We use a constraint on the natural frequency which we can directly relate to the attenuation at f_c, and another constraint on the angle between the real and imaginary parts of the poles, that will directly impact on the damping.

In order to be able to solve the LMI problem, we define $K = YW^{-1}$, where W and Y are the actual variables the solver finds and the ones we can play with. Which leads to:

$$L_f = \frac{1}{Y_2 W_{11} - Y_1 W_{12}}; \quad R_L = \frac{Y_1 W_{22} - Y_2 W_{12}}{Y_2 W_1 1 - Y_1 W_{12}} \tag{6}$$

The fact that L_f and R_L do not depend linearly on the terms of Y and W means that we can't directly optimize on them. The procedure taken involves a weighted optimization function on the terms of Y and W with a search for the optimal weight values.

Taking the same initial conditions as before and using the damping factor as a constraint, we obtain values of $L = 2.62\ \mu H$ and $R_L = 32\ m\Omega$ with a damping ratio of $\zeta = 0.31$ and an efficiency of $97\ \%$.

Using the numerical method we can also change some of the conditions while still ensuring stability. It's also possible to put multiple conditions and the more restrictive will be the one to shape the result.

For example instead of using the damping as a constraint we can use the settling time, we can design for a maximum settling time of $0.5\ ms$ and the results obtained are: $L = 2.73\ \mu H$ and $R_L = 71\ m\Omega$ and an efficiency of $94\ \%$. We can see that such (more restrictive) constraint implies a higher resistance and hence overall efficiency.

4. Conclusions

For a simple case of a filter + simplified converter, we have been able to rewrite the problem in order to be solved by numerical tools. The results between both, the conventional method and numerical method are very similar, this is a good result for such a simplified test.

Although the proposed case is simple and can be solved analytically, future work will be directed to numerically solving more complex systems. The main goal is to take advantage of the uncertainty robustness given by the polytopic model, the ensured stability of the method and the faster design times.

References

[1] R. W. Erickson and D. Maksimovic, *Fundamentals of Power Electronics 2nd Edition*, February. 2008, ISBN: 0306480484. DOI: 10 . 1017 / CBO9781107415324 . 004. arXiv: arXiv : 1011.1669v3.

[2] M. Chilali and P. Gahinet, "Design with Pole Place Constraints: An LMI Approach," *Ieee Transactions on Automatic Control*, vol. 41, no. 3, pp. 358–367, 1996.

Testing the Flexibility of a WO_3-Pd Gas Sensor under Automated Bending

Miriam Alvarado[1], Silvia De La Flor[2], Eduard Llobet[1], Alfonso Romero[1] and José Luis Ramírez[1]

[1] Departament d'Enginyeria Electrònica, Elèctrica i Automàtica, ETSE, Universitat Rovira i Virgili,
[2] Departament d'Enginyeria Mecànica, ETSEQ, Universitat Rovira i Virgili
Correspondence: joseluisramirez@urv.cat

Abstract

This work demonstrates the fabrication of flexible gas sensors based on metal oxides. The flexibility of the sensors was evaluated through cyclic mechanical bending test. The gas sensing performance of the devices was evaluated before and after having undergone mechanical bending test. The sensors were fabricated using a polyimide substrate, using gold inkjet-printed electrodes and an active layer of Pd decorated WO_3 nanowires. The sensors were subjected to 50 bending cycles under a compression force.

1. Introduction

Flexible sensors are a promise for diverse application fields such as personal environmental monitoring, training and sports or healthcare and medicine. These applications involve using wearable sensors, which are attached to the body or clothes to sense different parameters, especially gases. The use of flexible substrates improves the performance of these systems [1]. However, often no or little information is given on reliability. In this work, gas sensors employing metal oxide nanowires were developed using a flexible substrate and the effects of mechanical bending in their performance were studied.

2. Methods and Materials

The sensors were fabricated using a polymeric substrate (polyimide), a metallic transducer and a Pd decorated WO_3 active layer. The transducer was inkjet-printed using nanoparticle gold ink. The Pd decorated WO_3 active layer was obtained by means of Aerosol Assisted Chemical Vapor Deposition (AA-CVD).

A gas detection test was performed before and after subjecting the sensors to the bending test to evaluate their performance and reliability.

For the bending test, an electromechanical universal testing machine (Shimadzu AGS-X 10kN) was used. One sensor was tested at a time. The sensor was gripped from its top and bottom parts. To cause and out-of-plane bending due to buckling, the machine exerted a compression force. Meanwhile, the instantaneous electrical resistance of the sensor was measured.

3. Results

The AA-CVD process resulted in the direct growth onto the transducer of WO_3 nanowires decorated with Pd. Figure 1 shows the fabricated sensor. Sensors were tested against H_2 exposure before and after a 50-cycles bending test. For both measurements, three cycles of three concentrations (100, 200 and 300 ppm) of H_2 were tested, at a heater mean temperature of 100 °C.

Figure 2 shows the gas sensing response before and after the bending test. As can be observed, the response after bending increased, but the shape of the calibration curve remains identical.

Concerning to the bending test, the superior grip moved continuously at 20 mm/min, 1 mm up and down, 50 times, producing a maximum deflection of 1.47 mm. When the sensors were under their maximum deflection, they suffered an out-of-plane deformation due to buckling. A buckling deformation process is considered an unstable dynamic mode [2]. Besides, the cyclic loading imposed may well be associated with functional fatigue. This mode of fatigue, unlike traditional structural fatigue, does not lead to the failure of the device but could significantly limit its service life. The electrical resistance of the sensor increased by about 12% while the sensor was under maximum deflection. After the 50-cycles bending, the sensor resistance had a permanent increase of about 10%. Figure 3 shows the relative increments of the sensor resistance during the bending test.

4. Conclusions

We have proved that it is possible to produce reliable flexible sensors with a very affordable technology. The bending test demonstrated that the fabricated sensors can withstand harsh bending conditions and afterwards

remain fully functional for gas sensing.

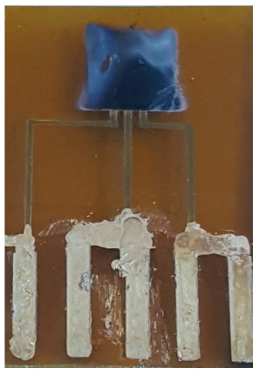

Fig.1. Pd-decorated WO_3 sensor with a size of 18 x 15 mm and a sensing area of 4 x 2 mm.

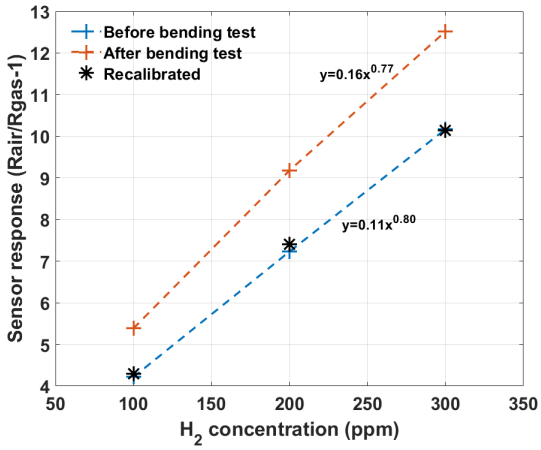

Fig.2. Hydrogen response of Pd-decorated WO_3 sensor before and after having undergone bending test.

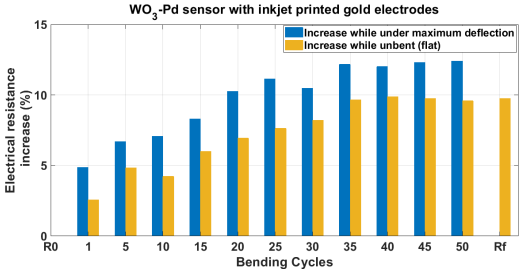

Fig.3. Changes in the relative sensor resistance during the bending test.

References

[1] A. Nag, S. C. Mukhopadhyay, and J. Kosel, "Wearable Flexible Sensors : A Review," *IEEE Sens. J.*, vol. 17, no. 13, pp. 3949–3960, 2017, doi: 10.1109/JSEN.2017.2705700.

[2] C. M. Wang, C. Y. Wang, and J. N. Reddy, *Exact Solutions for Buckling of Structural Members*. Boca Raton, FL, USA: CRC Press, 2004.

Engineering of Photonic Crystals by Gaussian Pulse Anodization based on Nanoporous Anodic Alumina

Laura K. Acosta, Elisabet Xifre-Perez, Josep Ferré-Borrull and Lluis F. Marsal*

*Departament d'Enginyeria Electrònica, Elèctrica i Automàtica, Universitat Rovira i Virgili, Avinguda Països Catalans 26, 43007 Tarragona, Spain. *Corresponding author e-mail address: lluis.marsal@urv.cat*

Abstract

This study presents a Gaussian pulse anodization approach to generate nanoporous photonic crystals with highly tunable and controllable optical properties across the visible–NIR spectrum. Nanoporous anodic alumina Gaussian photonic crystals (NAA-PCs) are fabricated in oxalic acid electrolyte by Gaussian pulse anodization –a novel form of pulse-like anodization. The effect of the Gaussian pulse width in the anodization profile on the optical properties of these photonic crystals is assessed by systematically varying this fabrication parameters

1. Introduction

Photonic crystals (PCs) are optical structures with allowed and forbidden photonic bands that modify the flow of photons when these travel across the PCs' structure. These light–matter interactions can be tuned with accuracy by engineering the PC's structure, which features regularly distributed regions of high and low refractive index in one, two, or three spatial dimensions (1-3) PCs can be produced with different architectures and materials to attain versatile light control across the broad range of spectral regions (from UV to IR) for specific applications, including photonic encoding9, chemical sensing and biosensing, lasing, and photocatalysis (4,7). Since the pioneering works by Masuda and co-workers, nanoporous anodic alumina (NAA) has long been envisaged as an ideal base material for developing nanoporous PCs due to its cylindrical nanopores with well-defined and highly controllable geometric features. NAA is formed by electrochemical oxidation of aluminum, a cost-effective and fully scalable process compatible with conventional micro- and nanofabrication. (8-10)

2. Materials and Methods

Materials

High purity Aluminium foils (thickness 0.5 mm and purity 99.99%), Ethanol (C_2H_5OH), perchloric acid ($HClO_4$), oxalic acid ($H_2C_2O_4$), hydrochloric acid (HCl), copper chloride ($CuCl_2$) and D-glucose ($C_6H_{12}O_6$) were purchased from Sigma-Aldrich. Double deionized water (DI) (18.6 MΩ) was used for all the solutions unless other specified.

Fabrication

First Al substrates were degreased in acetone, cleaned with ethanol and DI water and finally dried under steam of air. Before the anodization, Al substrates were electropolished in a mixture of Ethanol and Perchloric acid 4:1 at 20 V and 5ºC for 5 min. During the electropolishing step the stirring direction was alternated every 60 s. After the electropolishing the samples were cleaned with ethanol and DI water and dried under steam of air [4]. Then, the anodization was carried out in $H_2C_2O_4$ 0.3 M at 5ºC applying a Gaussian current profile with several design parameters like offset current m (I_0), amplitude current (I_1), Period (T), width of the Gaussian pulse (C) and number of periods (N). Figure 1 shows the Gaussian current profile and involved parameters during the fabrication.

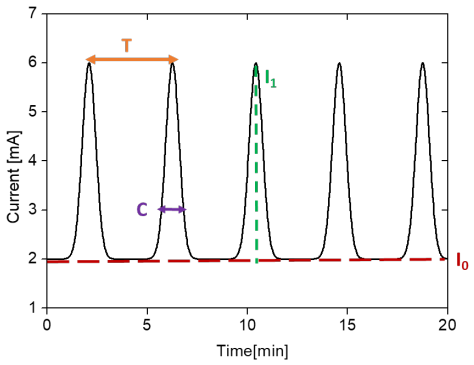

Figure 1. Gaussian current profile of Photonic Crystals based on nanoporous and alumina and involved fabrication parameters.

3. Results

Figure 2 shows the reflectance spectra of the different samples varying the C parameter (C = 5, 10, 20, 30 and 40) which feature narrow characteristic PSBs with an average full width at half maximum ($FWHM_{PSB}$) of 21 ± 9 nm. It is apparent that the position of the PSB red-shifts with increasing C following a linear dependence, in which λ_{PSB} red-shifts at a rate of 9.8 ± 0.3 nm s^{-1} with C. It can observed that NAA-PCs produced with C = 20 s achieve the maximum intensity (~80%), whereas those NAA-PCs produced with C = 5 s have the lowest intensity (~10%).

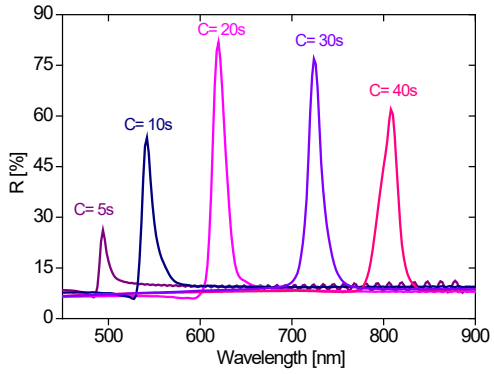

Figure 2. Reflection spectra on Gaussian photonic crystals varying the C parameter from 5 to 40 s

The ability to detect a change in refractive index of the medium filling the pores has been investigated by real-time spectroscopy. To this end, the sample is mounted in a sealed cell with a transparent window that permits the measurement of the reflectance spectrum by a fiber mini spectrometer as different fluids are injected to the cell and fill the staked structure NAA pores. **Figure 3** shows linear correlation between the concentration of D-glucose and the red shift of the PSB of the Gaussian PCs for the sample with C = 40 s It can be seen that the peak wavelength shifts linearly towards higher values for increasing glucose concentrations, with a lower limit of detection.

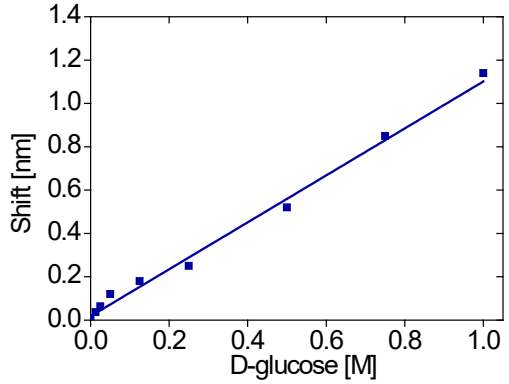

Figure 3. Linear correlations summarizing the dependence between λPSB in NAA-PCs (C = 40 s) and the D-glucose concentration

4. Conclusions

In this work, we fabricated photonic crystals based in nanoporous anodic alumina using a novel pulse-like anodization approach consisting of current density Gaussian pulses. The effect of the Gaussian pulse width on the optical features of the characteristic photonic stopband of these nanoporous PCs –position of central wavelength, full width at half maximum, reflection intensity and quality factor. The position of the PSB of these PCs can be precisely tuned varying by the width of the Gaussian pulse, from λPSB = 494 nm to 820 nm from C = 5 to 40 s, respectively The potential applicability of these PC structures as optical platform for sensing applications was evaluated by monitoring in real-time spectral shifts in their characteristic PSB upon selective infiltration of their medium with analytical solutions of D-glucose. Our observations indicate that NAA-GPCs can achieve high optical sensitivity.

Acknowledgements

This work was supported by the Spanish Ministerio de Ciencia, Innovación y Universidades (MICINN/FEDER) RTI2018-094040-B-I00, by the Agency for Management of University and Research Grants (AGAUR) ref. 2017-SGR-1527.

References

[1] A. Santos, J. Mater. Chem. C, 5, 5581 (2017).
[2] Laura K. Acosta, Francesc Bertó-Roselló, E. Xifre-Perez, Abel Santos, J. Ferré-Borrull. L.F. Marsal, Materials ACS Appl. Mater. Interfaces, 11, 3360 (2019).
[3] Lim, S. Y.; Law, C. S.; Markovic, M.; Kirby, J. K.; Abell, A. D.; Santos, A.. ACS Appl. Mater. Interfaces 2018, 10 (28), 24124–24136.
[4] Laura K. Acosta, Francesc Bertó-Roselló, E. Xifre-Perez, Cheryl Suwen Law, Abel Santos, J. Ferré-Borrull. L.F. Marsal, Materials. ACS Appl. Mater. Interfaces, 12, 19778-19787 (2020).
[5] G. Macias, L.P. Hernández-Eguía, J. Ferré-Borrull, J. Pallares, L.F. Marsal, ACS Appl. Mater. Interfaces, 5 (2013) 8093. [5] J. Ferré-Borrull, J. Pallarès, G. Macias, L.F. Marsal, Materials, 2014, 7, 5225-5253.
[6] G. Macias, J. Ferré-Borrull, J. Pallares, L.F. Marsal, Nanoscale research letters, 9 (2014) p. 315
[7] A. Santos, J.H. Yoo, C. Vashisth, T. Kumeria, Y. Wang, D. Losic, Nanoscale, 8 (2016) 1360.
[8] J. Ferre-Borrull, J. Pallares, Macías G, L.F. Marsal, Materials, 7, 5225 (2014).
[9] A Santos, L Vojkuvka, M Alba, VS Balderrama, J Ferré-Borrull, J Pallarès, physica status solidi, 209 (10), 2045-2048, (2012)
[10] A Santos, J Ferré-Borrull, J Pallarès, LF Marsal physica status solidi (a) 208 (3), 668-674 (2011)

Benzene Detection Employing Graphene decorated with $MAPbBr_3$ Nanocrystals

Juan Casanova-Chafer[1], Rocio Garcia-Aboal[2], Pedro Atienzar[2] and Eduard Llobet[1*]

[1] MINOS research group, Universitat Rovira i Virgili, 43007 Tarragona, Spain
[2] Instituto de Tecnología Química, CSIC-UPV, Universitat Politècnica de València, 46022 Valencia, Spain
[*] Corresponding Author: eduard.llobet@urv.cat

Abstract

We report the sensing performance of graphene nanolayers decorated with perovskite nanocrystals. In particular, $MAPbBr_3$ were employed. Thus, gas sensing devices were developed by using this nanomaterial, obtaining ultra-fast sensors (responses in 1-minute) able to work at room temperature. Therefore, the approach proposed here paves the way towards the development of low-cost and ultra-low power consumption devices.

1. Introduction

Despite graphene shows outstanding electronic and physicochemical properties to be employed as a gas sensor, its implementation in commercial devices still faces many issues. The main drawbacks that are limiting real applications are the low sensitivity and selectivity towards gas molecules of graphene in its pristine form. In consequence, further modifications are needed to enhance these essential gas-sensing parameters. One of the easiest and most effective strategies is the decoration of graphene (or other carbon nanomaterials) with metal or metal-oxide nanoparticles [1], an approach that has been extensively studied by many researchers.

In contrast, perovskites are promising materials that despite showing rich surface chemistry have attracted limited research interest for gas sensing until now. Probably because of their inherent problems, such as high degradation in contact with ambient moisture or their stability problems even at moderate working temperatures. Nevertheless, we recently reported the first use of graphene loaded with perovskite nanocrystals [2] to detect NO_2 and NH_3. Our approach has been demonstrated as a novel option to employ perovskites in dry and humid air, instead of their use in inert atmospheres by employing nitrogen without ambient moisture [3]. Here we deepen our study by analyzing, for the first time, the sensing performance of graphene decorated with perovskite nanocrystals towards volatile organic compounds (VOCs) detection.

2. Method

A chemical-sensitive film composed by graphene nanolayers loaded with perovskite nanocrystals is developed. Considering the general formula of perovskites (ABX_3), we employed the perovskite nanocrystal $MAPbBr_3$ to develop a gas sensor. The perovskite synthesis was adapted from the method proposed by L. Schmidt et al [4]. In particular, 85 mg of oleic acid (OA) were added to 2 mL of 1-octadene (ODE). The solution was stirred and heated to 80°C. Afterwards, 33.5 mg of octylammonium bromide (OABr) were added. Subsequently, another solution was prepared, in this case 26.4 mg and 18.3 mg of methylammonium bromide (MABr) and lead (II) bromide (PbBr2) respectively, were dissolved in 200 µL of Dimethylformamide (DMF). The solution was stirred until complete dissolution. Finally, both solutions were mixed and cooled to 60°C, adding 5 mL of acetone to induce the immediate precipitation of the nanocrystals. Then, the solution was centrifugated at 6000 rpm for 10 minutes in order to extract the yellow precipitates. Afterwards, the precipitates were dispersed in Toluene.

Once the perovskite NCs were synthesized, a graphene solution in toluene was prepared by using graphene nanolayers. Afterwards, the solution was placed in an ultrasonic tip to apply a pulsed sonication for 90 minutes. Then, once the graphene is properly exfoliated, perovskite NCs were added (5% wt.) to the solution and the nanomaterials were mixed in an ultrasonic bath for 1 hour. Finally, the resulting graphene flakes decorated with perovskite NCs were deposited onto alumina substrates that comprised screen-printed platinum interdigitated electrodes by a spray pyrolysis technique.

3. Characterization

The nanomaterials employed in this work were characterized in depth employing techniques such as High-Resolution Transmission Electron Microscopy (HR-TEM) to analyze the nanocrystal size and its interplanar distances and Field Emission Scanning

Electron Microscope (FESEM) to evaluate the spatial nanocrystal distribution over the graphene nanolayers. Figure 1a shows nanocrystals with diameters below to 10 nm, which are found suitable for the decoration of graphene Figure 1b.

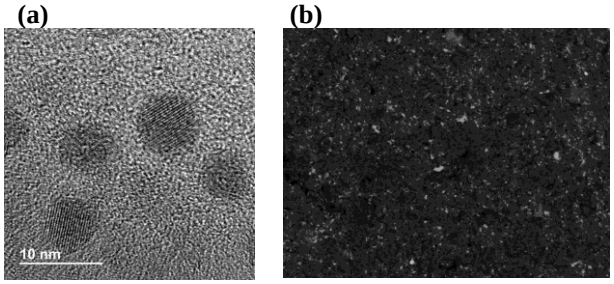

Figure 1. (a) High-Resolution Transmission Electron Microscope (HRTEM) images of $MAPbBr_3$. (b) Field Emission Scanning Electron Microscope (FESEM) image recorded with Back-Scattered Electron (BSE) detector. Bright spots correspond to the perovskite NCs, meanwhile, black background corresponds to graphene.

Afterwards, the film developed was integrated in gas sensing devices, which are placed in an airtight Teflon chamber connected to a calibrated bottle of benzene. Consecutive gas dilutions are performed in order to register the responses to different analyte concentrations.

4. Results

Graphene loaded with $MAPbBr_3$ perovskite NCs was exposed to continuous response and recovery cycles of 2, 4, 6 and 8 ppm of VOCs. An example of the electrical responses registered upon the exposure to benzene vapours is shown in Figure 2. Gas exposure was limited to 1 min, meanwhile baseline recovery was limited to 5 min in dry air.

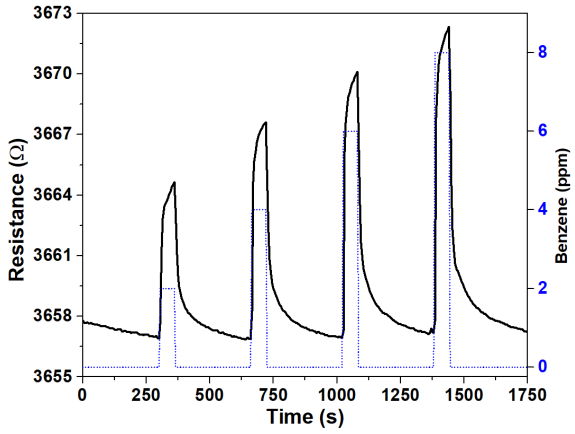

Figure 2. Resistance changes (black line) for graphene loaded with perovskite NCs under the exposure to increasing concentration of benzene (blue dashed line).

Since it is well known that graphene-based chemiresistors show very weak and very slow response to gas molecules. With their decoration employing perovskite NCs, highly reproducible and ultra-fast responses were obtained. Also, a suitable reversibility has been shown.

5. Conclusions

Gas sensors composed by graphene decorated with perovskite nanocrystals were successfully employed to detect VOCs such as benzene at ppm levels. Therefore, the device developed achieve an ultrafast and highly reproducible detection of gases, even when it's operated in room temperature conditions. Also, the low noise level showed indicate that trace detection of VOCs at ppb levels would be possible. Thus, the approach proposed here leads to an inexpensive, reliable and low-power resistive sensors. Paving the way towards their implementation in ubiquitous air monitoring applications.

References

[1] J. Casanova-Cháfer, E. Navarrete, X. Noirfalise, P. Umek, C. Bittencourt, E. Llobet, Gas Sensing with Iridium Oxide Nanoparticle Decorated Carbon Nanotubes, Sensors. 19 (2019) 113.

[2] J. Casanova-Cháfer, R. García-Aboal, P. Atienzar, E. Llobet, Gas Sensing Properties of Perovskite Decorated Graphene at Room Temperature, Sensors. 19 (2019) 4563.

[3] C. Bao, J. Yang, W. Zhu, X. Zhou, H. Gao, F. Li, G. Fu, T. Yu, Z. Zou, A resistance change effect in perovskite $CH_3NH_3PbI_3$ films induced by ammonia, Chem. Commun. 51 (2015) 15426–15429.

[4] C. Schmidt, A. Pertegas, S. González-Carrero. O. Malinkiewicz, S. Agouram, G. Mínguez Espallargas, H. Bolink, R. Galian. Nontemplate Synthesis of $CH_3NH_3PbBr_3$ Perovskite Nanoparticles, JACS. 3 (2014) 136.

p-n heterojunction metal oxide gas sensors via AACV

Eric Navarrete[1], Eduard Llobet[1]*

[1]MINOS-EMaS, Universitat Rovira i Virgili, E-43007 Tarragona, Spain
*Correspondence: eduard.llobet@urv.cat; Tel.: +34-977-558-502

Abstract

Metal oxide based gas sensors are employed as gas sensors, among their advantages we could find good performance, long life-spawn and great sensitivity towards both oxidant and reductive gases. Despite that, they have a severe drawback; selectivity. Therefore, in this work we present the synthesis of localized n-p heterojunctions among a sensing layer with the aim to improve the selectivity of tungsten trioxide nanowires (WO_3 NWs) towards a specific gas.

WO_3 NWs, (n-type) were grown through an AACVD methodology. Subsequently, a loading with different p-type metal oxides was performed in order to create n-p heterojunctions with the aim of increasing the chemical and electric sensitization of the material. The WO_3 NWs were loaded with nickel oxide [1], cobalt oxide [2] and iridium oxide [3] as p-type nanoparticles. After the synthesis step; the unloaded nanowires, and loaded nanowires were employed as chemoresistive sensors and exposed to different gas atmospheres and the results compared. Table 1 summarizes the results obtained.

1. Introduction

Anthropogenic gas pollutants global emissions have exponentially risen in the few past decades. Therefore, there is a clear need in researching and developing nanosized metal oxides gas sensors which are both sensitive and selective as well as inexpensive. Here we focus on the growth, through aerosol assisted chemical vapor deposition, of n-type WO_3 nanowires loaded with either p-type nickel oxide nanoparticles, cobalt oxide nanoparticles or iridium oxide nanoparticles. The objective is to achieve both chemical and electronic sensitization effects to achieve sensitive and potentially selectivity to different types of gases. Different routes are explored to effectively achieve a wide range of decoration loading in order to obtain the most optimal conditions to perform gas analysis. Ni loading, displayed good results towards H_2S sensing, cobalt oxide displayed a good behavior towards ethanol and ammonia and finally iridium oxide was tested for NO_2 detection with outstanding results.

2. Material Synthesis

The WO_3 nanowires were synthesized via aerosol assisted chemical vapor deposition methodology. In order to obtain the NWs, an organic solution consisting on acetone : methanol, ratio 3:1, was prepared and 50 mg $W(CO)_6$ were dissolved into it. When the solution was ready, it was placed inside a high-frequency wave generator and the liquid phase was brought into a spray form. The spray then was carried by a flow of an inert gas, N_2, at 1 L/min towards a preheated hot-wall reactor at 400 ºC. Prior the reactor heating, an alumina transducer were the NWs synthesis and growth would take place was placed inside. The synthesis step typically lasted from 25 to 30 min. Finally, the reactor was cooled down naturally to room temperature. The NWs layer obtained through this methodology displayed a deep-blue color indicative of a non-stoichiometric WO_3 and the presence of remnant amorphous carbon due to the burned organic compounds. In order to further increase the oxidation and remove the remnant carbon an annealing step is performed at 500 ºC during 120 minutes with a 5 ºC/min heating ramp under 1 L/min synthetic dry air flow. After the annealing the NWs layer displayed a pale-yellowish color indicative of quasi-stoichiometric WO_3 NWs.

In order to produce heterojunctions, the nanowires were decorated with different materials, nickel oxide, cobalt oxide and iridium oxide nanoparticles. To achieve such decorations, AACVD methodology was employed. For each of the decorations a solution was prepared employing 10 ml methanol were either, nickel acetylactonate, cobalt acetylacetonate or idium oxide nanopowder were dissolved. Different concentrations were assessed in order to obtain the suitable concentrations for gas sensing porpoises. The loading was performed in equal terms as the NWs synthesis and a second annealing step was also performed.

3. Characterization and gas sensing results

All the sensors were thoroughly studied by means of SEM, HR-TEM, XRD, XPS, PL and ToF-SIMS. figure 1 shows the typical shape and morphology of pure WO_3 NWs. The nanowires present a well-defined structure with an average length of 16 µm and a diameter comprised between 50 to 100 nanometers. The WO_3 NWs obtained are single crystalline with a monoclinic structure matching with the ICDD 431035 card.

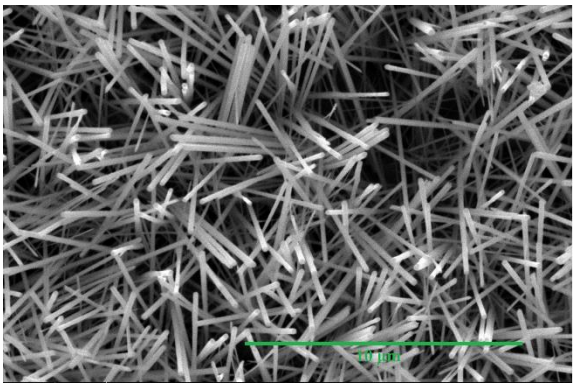

Figure 1. WO_3 NWs surface gown atop of an alumina transducer.

The sensors WO_3 pure and loaded WO3 were tested under different gas streams inside a Teflon gas chamber. The sensors performance as gas sensors was tested through a series of different gases at diverse concentrations under dry air conditions. The experiment was set as 30 minutes pulses, in which each pulse consisted on shifting synthetic air with a target gas. The steps were designed in order to expose the sensor, clean it with air and exposing it again to a higher gas concentration as shown in figure 2.

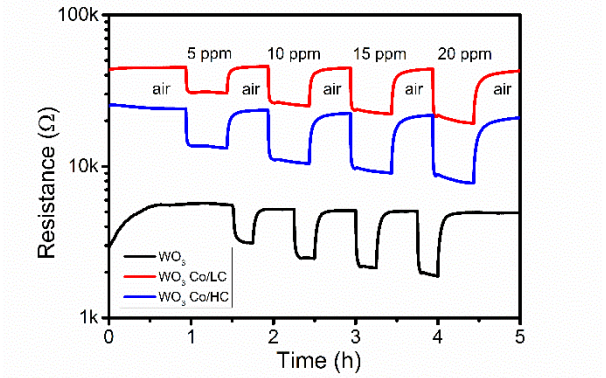

Figure 2. Typical data set obtained when sensors are exposed towards a target gas. This figure shows the resistance behaviour of pure and cobalt loaded nanowires towards the increasing concentrations of ethanol.

Different temperatures, (150, 200 and 250ºC), were also tested in order to determine which the best operando conditions for each gas tested was. The gases tested were H_2S, H_2, EtOH, NH_3, NO_2 and CH_4. Table 1 summarizes the best responses and the increase of the responses when heterojunctions are present.

Table 1: Experimental Conditions and Relative values comparison towards a specific gas.

Loading	T / °C	Target Gas	Loaded Sensitivity [a](R_{air}/R_{gas}); [b](R_{gas}/R_{air})	Pure Sensitivity [a](R_{air}/R_{gas}); [b](R_{gas}/R_{air})
NiO	250	50 ppm H_2S	13[a]	3[a]
Co_xO_y	250	25 ppm NH_3	12[a]	5[a]
IrO_x	200	250 ppb NO_2	100[b]	1.5[b]

Furthermore, for each of the decorations tested the mechanism regarding the boast in the sensing response were also discussed and assessed.

7. Conclusions

Heterojunction nanomaterials between tungsten trioxide nanowires (n-type) and transition metal oxides (p-type) nanoparticles have been successfully synthetized through AACVD in a two-step procedure. The material characterization confirmed in all cases the high crystallinity and the homogenous distribution of decorating nanoparticles for the different cases studied. In particular, the synthesis of heterojunctions has proven to be an inexpensive, simple and versatile procedure to overcome semiconductor metal oxide lack of selectivity by boosting the response towards a specific target gas, meanwhile the response to the other gases remains almost unaffected.

References (Times 10 bold)

[1] E. Navarrete, C. Bittencourt, P. Umek, and E. Llobet, “AACVD and gas sensing properties of nickel oxide nanoparticle decorated tungsten oxide nanowires,” J. Mater. Chem. C, vol. 6, no. 19, 2018.

[2] È. Navarrete, C. Bittencourt, X. Noirfalise, P. Umek, E, Gonzalez, F. Güell and E. Llobet, “WO3 nanowires loaded with cobalt oxide nanoparticles, deposited by a two-step AACVD for gas sensing applications,” Sensors Actuators, B Chem., vol. 298, 2019.

[3] E. Navarrete, C. Bittencourt, P. Umek, D. Cossement, F. Güell, and E. Llobet, “Tungsten trioxide nanowires decorated with iridium oxide nanoparticles as gas sensing material,” J. Alloys Compd., vol. 812, 2020.

Single-step CVD synthesis of layered WS_2 films for NO_2 gas sensing

Aanchal Alagh, F.E. Annanouch, E. Llobet
(MINOS-EMaS), Department of Electrical Electronic Engineering and Automation
Universitat Rovira i Virgili, Tarragona, Spain
alagh.aanchal@urv.cat, fatimaezahra.annanouch@urv.cat, eduard.llobet@urv.cat

Abstract

Recently layered inorganic materials analogues to graphene such as two-dimensional transition metal dichalcogenides (2D TMDs) have emerged as promising building blocks for the gas sensing industry. Indeed, they show impressive semiconducting properties, tunable band gap, large surface area and excellent gas adsorbing capacities. Herein, we report for the first time, on a single step synthesis of 3D assembly of layered WS_2 sensing material, via hydrogen free, atmospheric pressure CVD technique, directly on silicon oxide substrate for NO_2 resistive gas sensing application. E-SEM, EDX and Raman spectroscopy were used to investigate the morphology and composition of the grown material. Demonstration of WS_2 sensor towards one of the most pollutant gases (NO_2) showed promising results with high sensitivity and low detection limit below 20 ppb.

Introduction

Advancement in the chemical, pharmaceutical, automotive industries, petroleum production and so forth, all have added extraordinary advantages to our current way of life. However, with improvement of these enterprises, various toxic gases at trace levels are consistently emitted in the environment, which has impact and have adverse effects on human health. For instance, NO_2 (nitrogen dioxide) has direct contribution in the formation of fine particulate matter (PM), ground level ozone and acid rain which is highly detrimental for the environment. Thus, there is a growing need to fabricate highly sensitive and selective NO_2 sensors with fast responses, low detection limit and low-cost fabrication.

Post graphene, atomically layered two-dimensional (2D) transition metal dichalcogenide materials have received considerable attention from researchers worldwide and have shown great potential especially in the gas sensing industry with high sensitivity and provides interesting new possibilities for sensor processing. Among various 2D TMDs material available, WS_2 has attracted major attention as it offers high compatibility for integration with conventional Si (silicon) technology with superior semiconducting properties, inherent flexibility, high surface to volume ratio and low power consumption[1].

In this work, we report on growing 3D assembly of layered WS_2 by a single step hydrogen free atmospheric pressure CVD technique. To the best of our knowledge, resistive gas sensor using as grown layered WS_2 material, synthesized from CVD routes has not been yet reported. It is observed that the growth is highly influenced by various growth parameters such as distance between the two precursors, WO_3 (tungsten trioxide) and S (sulphur), their concentration, position of the substrate, temperature inside the growth chamber, gas flow rate and deposition time. Hence, several depositions were tried to optimise these parameters until a continuous film of layered WS_2 is achieved. After that a traditional lab-made sensor was fabricated and characterized towards different concentrations of NO_2. We have observed impressive results where the sensor is able to detect ppb's (parts per billion) level of nitrogen dioxide, while more gases such as ammonia, hydrogen sulphide which are toxic for human health and harmful for the environment will be investigated in near future.

Results

WS_2 films were grown by atmospheric pressure CVD without the assistance of hydrogen gas, using a two-temperature zone furnace as depicted in Fig.1, the prepared sensor is depicted in Fig.2.

Fig. 3 depicts SEM images of as deposited layered WS2 films on Si/SiO2 substrate. These films grown at 900°C, comprises of triangular domains of WS_2 with an average size of ~ 6µm. Fig. 3a clearly demonstrates the formation of 3D assembly of the WS_2 grown. Whereas Fig. 3b shows that the grown WS_2 flakes are atomically thin with isolated perfect triangles (fig 3 b and c). The fine triangular shape with clean surface and smooth edge indicates growth of high quality WS_2 crystals.

Raman spectrum plays a key role to identify the number of layers present. Fig. 4 corresponds to the Raman spectrum obtained, and here the strongest peak at ~ 419 cm^{-1} corresponds to presence of multi-layered WS_2 [2]. It is observed that some of the WS_2 domains were monolayer whereas most of the domains were multilayer.

Furthermore, Fig. 5 shows the gas sensing results of WS_2 sensor towards 50 and 20 ppb of NO_2 respectively. Gas sensing results show that WS_2 sensor behaves as an n-type semiconductor material: decreasing resistance

when exposed to air and increasing resistance when exposed to oxidising gas NO_2 and vice-versa. The sensor showed high sensitivity with good repeatable responses towards target gas. the response was calculated to be 17.5% and 2.5% towards 50 ppb and 20 ppb of NO_2 gas respectively. This indicates that the detection limit is below 20 ppb. In contrast, it is clear that the signal is noisy, and this can be related to the traditional electrodes used in this work (as shown in Figure 2 b).

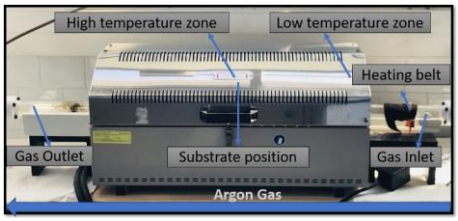

Figure 1 Deposition furnace (Atmospheric Pressure Chemical Vapour Deposition)

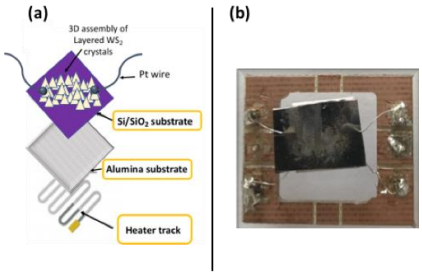

Figure 2 WS_2 sensor

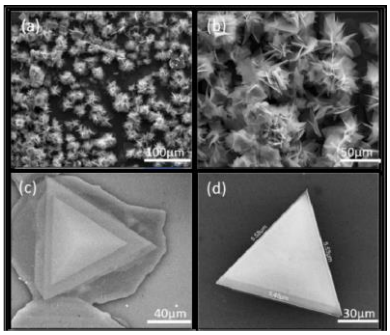

Figure 3 SEM images showing the morphology of the layered WS_2 films grown (a) 3d assembly of WS_2 at 100µm,(b) 50µm (c) atomically thin triangular flake at 400µm (d) triangular flake with each dimension ~ 6µm

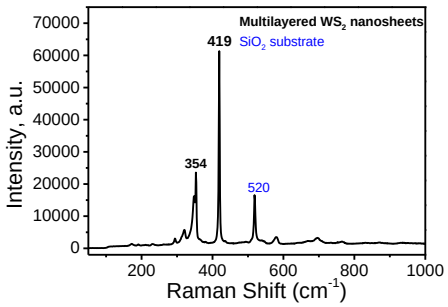

Figure 4 Raman spectrum of the multi-layered WS_2

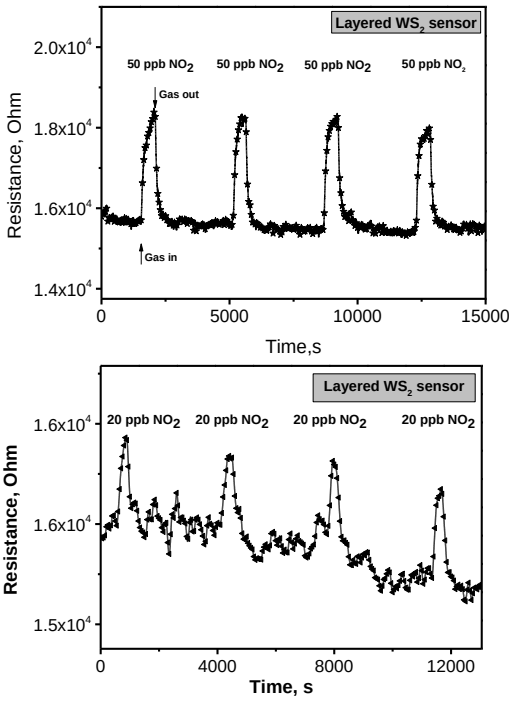

Figure 5 WS_2 sensor response towards 50 and 20 ppb of NO_2 gas at 250ºC

Conclusion

3D assembly of layered WS_2 films were successfully deposited on silicon oxide substrate, using a hydrogen free, single step atmospheric pressure CVD approach. The obtained material was used for the first time as a resistive NO_2 gas sensor. The results revealed that layered WS_2 led to the fabrication of a highly sensitive NO_2 sensor with a detection limit below 20ppb. The measurements at such low nitrogen dioxide concentration showed some noise, however, this could be optimized further by ameliorating the electrodes used in this work. Thus, in the near future, improvement of the transducer design will be studied, and more toxic gases will be tested.

Acknowledgment

This project has received funding from the European Union's Horizon 2020 research and innovation programme under the Marie Skłodowska-Curie grant agreement No. 713679.

References

[1] A. Alagh, F. E. Annanouch, E. Llobet, U. R. I. Virgili, and A. P. Catalans, "Single-step CVD synthesis of layered WS 2 films for NO 2 gas sensing," *2019 IEEE SENSORS*, no. 2, pp. 1–4, 2020.

[2] K. M. McCreary, A. T. Hanbicki, G. G. Jernigan, J. C. Culbertson, and B. T. Jonker, "Synthesis of Large-Area WS 2 monolayers with Exceptional Photoluminescence," *Sci. Rep.*, vol. 6, no. August 2015, pp. 1–7, 2016.

Synthesis of new *small* molecules as Hole Transporting Materials for High-Performance Perovskite Solar Cell

Dora González-Ruiz*[a,b], Ece Aktas[a,b] and Emilio Palomares[a,c,d]

[a]*Institute of Chemical Research of Catalonia (ICIQ), Avinguda del Països Catalans 16, 43007 Tarragona, Spain.*
Tel: +34 977 920 200; E-mail: dagonzalez@iciq.es
[b]*Universitat Rovira i Virgili (URV), N5- Edifici de Serveis Centrals Carrer Marcel·lí Domingo, 2-4-6, 43007- Tarragona*
[c]*Catalan Institution for Research and Advanced Studies (ICREA), Passeig de Lluis Companys 23, 08010 Barcelona, Spain.*
[d]*Universidad de Pau y Pays de l'Adour (UPPA), Avenue de l'Université, 64012 Pau, Francia*
Teléfono: +33 5 59 40 70 00.

Abstract

Perovskite solar cells (PSCs) has attracted many attention due to its high efficiencies achieved and its low-cost fabrication procedures, it's considered to be a promising candidate as renewable energy source. 2,2′7,7′-tetrakis- (N,N-di-p-methoxyphenyl-amine)-9,9′-spirobifluorene (Spiro-OMeTAD) is the most used hole transporting material (HTM) for PSCs, reaching efficiencies up to 24.2 %[1]. However, its production cost, relative low hole mobility and difficult synthetic pathway with low yield are disadvantages that point out the need of designing and synthetizing new HTMs[2]. In this work, we report the synthesis of a carbazole-based novel HTM for PSCs.

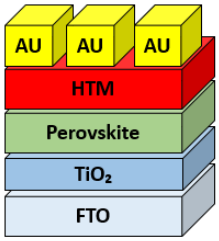

1. Introduction

A variety of hole transporting materials alternatives have been synthesized, in order to improve on the efficiency and stability of PSCs using other HTMs rather than Spiro-OMeTAD. HTMs based on the carbazole moiety (Scheme 1) have attracted attention due to their chemical structure has versatile and advantageous characteristics such as the low cost of the starting material (9H-carbazole), good chemical stability, easy functionalization and high solubility in common solvents among others[3].

2. HTM

The role of HTM in PSCs is extracting holes created in the perovskite when it absorbs light and transporting them towards the gold electrode (Au)[3]. For this reason, the principal characteristics that have to present a good HTM are: high hole mobility, good thermal and photochemical stability, energy levels (highest occupied molecular orbital, HOMO and the lowest unoccupied molecular orbital, LUMO) that fit with perovskite's, good photovoltaic parameters like large photocurrents, high open circuit voltage or fill factor and high solubility in common solvents[4].

Due to the optimal properties we mentioned before, a carbazole-based HTM was synthetized using a bithiophene as bridge (DREA-02), shown in (Scheme 1).

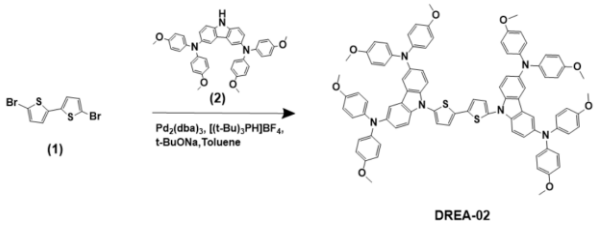

Scheme 1: Synthetic pathway for DREA-02.

3. Results and conclusions

The reactions involved in the synthesis of DREA-02 consisted first in a bromination with N-Bromosuccinimide (NBS) in DMF to obtain 5,5'-dibromo-2,2'-bithiophene (1). After that, (2), synthesized according to literature procedures[5]. Finally, the coupling of the unit using Buchwald-Hartwig amination was carried out using $Pd_2(dba)_3$ as a catalyst to obtain the desired product DREA-02.

Figure 2 show the ^{1}H NMR of DREA-02 data were in good agreement with the formula we report.

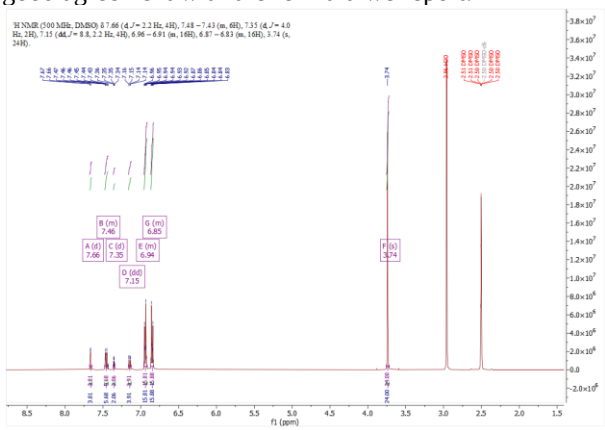

Figure 2. ^{1}H NMR (DMSO) of DREA-02.

Before using DREA-02 as HTMs in PSCs, it's needed to do a full characterization doing ^{13}C NMR, Mass Spectroscopy Absorption, Emission, cyclic voltammetry and other measurements like, TGA and DSC.

If the HOMO level is higher than the edge valence band of the perovskite and its LUMO level is high enough, we expect a similar or higher efficiency comparing with that of Spiro-OMeTAD.

4. References

[1] Kasparas Rakstys, Cansu Igci and Mohammad Khaja Nazeeruddin,"Efficiency vs. stability: dopant-free hole transporting materials towards stabilized perovskite solar cells", Chem. Sci., 2019, Advance Article.

[2] Ze Yu, Licheng Sun, "Recent Porgress on Hole-Transporting Materials for Emerging Organometal halide Perovskite Solar Cells", Adv. Energy Mater., 2015, 1500213.

[3] Sang Do Sung, Wan In Lee, "14.8% perovskite solar cells employing carbazole derivatives as hole transporting materials", Chem. Commun., 2014, 50, 14161-14163.

[4] Agarwala P, Kabra. "A review on triphenylamine (TPA) based organic hole transport materials (HTMs) for dye sensitized solar cells (DSSCs) and perovskite solar cells (PSCs): evolution and molecular engineering" J. Mater. Chem. A, 2017,5, 1348-1373.

[5] Xu, B; Sheibani, E.; Liu, P.; Zhang, J.; Tian, H.; Vlachopoulos, N.; Boschloo, G.; Kloo, L.; Hagfeldt, A.; Sun,L. "Carbazole-Based Hole-Transport Materials for Efficient Solid-State Dye-Sensitized Solar Cells and Perovskite Solar Cells" Adv. Mater. 2014, 26, 6629–6634.

[6] Adv. Mater. 2008, 20, 1357-1362.

[7] J. Mater. Chem. A, 2016,4, 15788-15822